# Search for New Cosmic-Ray Acceleration Sites within the 4FGL Catalog Galactic Plane Sources

S. Abdollahi, F. Acero, M. Ackermann, L. Baldini, J. Ballet, G. Barbiellini, D. Bastieri, R. Bellazzini, B. Berenji, A. Berretta, et al.

The Astrophysical Journal, 933:204 (29pp), 2022 July 10 https://doi.org/10.3847/1538-4357/ac704f


# Search for New Cosmic-Ray Acceleration Sites within the 4FGL Catalog Galactic Plane Sources

S. Abdollahi[1], F. Acero[2], M. Ackermann[3], L. Baldini[4], J. Ballet[2], G. Barbiellini[5,6], D. Bastieri[7,8,9], R. Bellazzini[10], B. Berenji[11], A. Berretta[12], E. Bissaldi[13,14], R. D. Blandford[15], R. Bonino[16,17], P. Bruel[18], S. Buson[19], R. A. Cameron[15], R. Caputo[20], P. A. Caraveo[21], D. Castro[22,20], G. Chiaro[21], N. Cibrario[16], S. Ciprini[23,24], J. Coronado-Blázquez[25,26], M. Crnogorcevic[27], S. Cutini[28], F. D'Ammando[29], S. De Gaetano[14], N. Di Lalla[15], F. Dirirsa[30], L. Di Venere[13,14], A. Domínguez[31], S. J. Fegan[18], A. Fiori[32], H. Fleischhack[33,20,34], A. Franckowiak[35], Y. Fukazawa[36], P. Fusco[13,14], V. Gammaldi[26], F. Gargano[14], D. Gasparrini[23,24], F. Giacchino[23,24], N. Giglietto[13,14], F. Giordano[13,14], M. Giroletti[29], T. Glanzman[15], D. Green[37], I. A. Grenier[2], M.-H. Grondin[38], S. Guiriec[39,20], M. Gustafsson[40], A. K. Harding[41], E. Hays[20], J. W. Hewitt[42], D. Horan[18], X. Hou[43,44,45], G. Jóhannesson[46,47], T. Kayanoki[36], M. Kerr[48], M. Kuss[10], S. Larsson[49,50,51], L. Latronico[16], M. Lemoine-Goumard[38], J. Li[52,77], F. Longo[5,6], F. Loparco[13,14], P. Lubrano[28], S. Maldera[16], D. Malyshev[53], A. Manfreda[4], G. Martí-Devesa[54], M. N. Mazziotta[14], I. Mereu[12,28], P. F. Michelson[15], N. Mirabal[20,55], W. Mitthumsiri[56], T. Mizuno[57], M. E. Monzani[15], A. Morselli[23], I. V. Moskalenko[15], E. Nuss[58], N. Omodei[15], M. Orienti[29], E. Orlando[59,15], J. F. Ormes[60], D. Paneque[37], Z. Pei[8], M. Persic[5,61], M. Pesce-Rollins[10], R. Pillera[13,14], H. Poon[36], T. A. Porter[15], G. Principe[6,5,29], S. Rainò[13,14], R. Rando[62,7,9], B. Rani[63,20,64], M. Razzano[4], S. Razzaque[65], A. Reimer[54,15], O. Reimer[54], T. Reposeur[38], M. Sánchez-Conde[25,26], P. M. Saz Parkinson[66,67,68], L. Scotton[58], D. Serini[13], C. Sgrò[10], E. J. Siskind[69], G. Spandre[10], P. Spinelli[13,14], K. Sueoka[36], D. J. Suson[70], H. Tajima[71,15], D. Tak[72,20], J. B. Thayer[15], D. F. Torres[73,74], E. Troja[20,27], J. Valverde[55,20], Z. Wadiasingh[20], K. Wood[75], and G. Zaharijas[76]

[1] IRAP, Université de Toulouse, CNRS, UPS, CNES, F-31028 Toulouse, France
[2] Université Paris Saclay and Université Paris Cité, CEA, CNRS, AIM, F-91191 Gif-sur-Yvette, France; jean.ballet@cea.fr
[3] Deutsches Elektronen Synchrotron DESY, D-15738 Zeuthen, Germany
[4] Università di Pisa and Istituto Nazionale di Fisica Nucleare, Sezione di Pisa I-56127 Pisa, Italy
[5] Istituto Nazionale di Fisica Nucleare, Sezione di Trieste, I-34127 Trieste, Italy
[6] Dipartimento di Fisica, Università di Trieste, I-34127 Trieste, Italy
[7] Istituto Nazionale di Fisica Nucleare, Sezione di Padova, I-35131 Padova, Italy
[8] Dipartimento di Fisica e Astronomia "G. Galilei", Università di Padova, I-35131 Padova, Italy
[9] Center for Space Studies and Activities "G. Colombo", University of Padova, Via Venezia 15, I-35131 Padova, Italy
[10] Istituto Nazionale di Fisica Nucleare, Sezione di Pisa, I-56127 Pisa, Italy
[11] California State University, Los Angeles, Department of Physics and Astronomy, Los Angeles, CA 90032, USA
[12] Dipartimento di Fisica, Università degli Studi di Perugia, I-06123 Perugia, Italy
[13] Dipartimento di Fisica "M. Merlin" dell'Università e del Politecnico di Bari, via Amendola 173, I-70126 Bari, Italy
[14] Istituto Nazionale di Fisica Nucleare, Sezione di Bari, I-70126 Bari, Italy
[15] W. W. Hansen Experimental Physics Laboratory, Kavli Institute for Particle Astrophysics and Cosmology, Department of Physics and SLAC National Accelerator Laboratory, Stanford University, Stanford, CA 94305, USA
[16] Istituto Nazionale di Fisica Nucleare, Sezione di Torino, I-10125 Torino, Italy
[17] Dipartimento di Fisica, Università degli Studi di Torino, I-10125 Torino, Italy
[18] Laboratoire Leprince-Ringuet, École polytechnique, CNRS/IN2P3, F-91128 Palaiseau, France
[19] Institut für Theoretische Physik and Astrophysik, Universität Würzburg, D-97074 Würzburg, Germany
[20] NASA Goddard Space Flight Center, Greenbelt, MD 20771, USA
[21] INAF-Istituto di Astrofisica Spaziale e Fisica Cosmica Milano, via E. Bassini 15, I-20133 Milano, Italy
[22] Harvard-Smithsonian Center for Astrophysics, Cambridge, MA 02138, USA
[23] Istituto Nazionale di Fisica Nucleare, Sezione di Roma "Tor Vergata", I-00133 Roma, Italy
[24] Space Science Data Center–Agenzia Spaziale Italiana, Via del Politecnico, snc, I-00133, Roma, Italy
[25] Instituto de Física Teórica UAM/CSIC, Universidad Autónoma de Madrid, E-28049 Madrid, Spain
[26] Departamento de Física Teórica, Universidad Autónoma de Madrid, E-28049 Madrid, Spain
[27] Department of Astronomy, University of Maryland, College Park, MD 20742, USA
[28] Istituto Nazionale di Fisica Nucleare, Sezione di Perugia, I-06123 Perugia, Italy
[29] INAF Istituto di Radioastronomia, I-40129 Bologna, Italy
[30] Astronomy and Astrophysics Research Development Department, Entoto Observatory and Research Center, Ethiopian Space Science and Technology Institute, Ethiopia
[31] Grupo de Altas Energías, Universidad Complutense de Madrid, E-28040 Madrid, Spain
[32] Dipartimento di Fisica "Enrico Fermi", Università di Pisa, Pisa I-56127, Italy
[33] Catholic University of America, Washington, DC 20064, USA
[34] Center for Research and Exploration in Space Science and Technology (CRESST) and NASA Goddard Space Flight Center, Greenbelt, MD 20771, USA
[35] Ruhr University Bochum, Faculty of Physics and Astronomy, Astronomical Institute (AIRUB), D-44780 Bochum, Germany
[36] Department of Physical Sciences, Hiroshima University, Higashi-Hiroshima, Hiroshima 739-8526, Japan
[37] Max-Planck-Institut für Physik, D-80805 München, Germany
[38] Université Bordeaux, CNRS, LP2I Bordeaux, UMR 5797, F-33170 Gradignan, France; lemoine@lp2ib.in2p3.fr, reposeur@lp2ib.in2p3.fr
[39] The George Washington University, Department of Physics, 725 21st St, NW, Washington, DC 20052, USA
[40] Georg-August University Göttingen, Institute for theoretical Physics—Faculty of Physics, Friedrich-Hund-Platz 1, D-37077 Göttingen, Germany
[41] Los Alamos National Laboratory, Los Alamos, NM 87545, USA
[42] University of North Florida, Department of Physics, 1 UNF Drive, Jacksonville, FL 32224 , USA
[43] Yunnan Observatories, Chinese Academy of Sciences, 396 Yangfangwang, Guandu District, Kunming 650216, People's Republic of China
[44] Key Laboratory for the Structure and Evolution of Celestial Objects, Chinese Academy of Sciences, 396 Yangfangwang, Guandu District, Kunming 650216, People's Republic of China

[45] Center for Astronomical Mega-Science, Chinese Academy of Sciences, 20A Datun Road, Chaoyang District, Beijing 100012, People's Republic of China
[46] Science Institute, University of Iceland, IS-107 Reykjavik, Iceland
[47] Nordita, Royal Institute of Technology and Stockholm University, Roslagstullsbacken 23, SE-106 91 Stockholm, Sweden
[48] Space Science Division, Naval Research Laboratory, Washington, DC 20375-5352, USA
[49] Department of Physics, KTH Royal Institute of Technology, AlbaNova, SE-106 91 Stockholm, Sweden
[50] The Oskar Klein Centre for Cosmoparticle Physics, AlbaNova, SE-106 91 Stockholm, Sweden
[51] School of Education, Health and Social Studies, Natural Science, Dalarna University, SE-791 88 Falun, Sweden
[52] CAS Key Laboratory for Research in Galaxies and Cosmology, Department of Astronomy, University of Science and Technology of China, Hefei 230026, People's Republic Of China
[53] Friedrich-Alexander Universität Erlangen-Nürnberg, Erlangen Centre for Astroparticle Physics, Erwin-Rommel-Str. 1, D-91058 Erlangen, Germany
[54] Institut für Astro- und Teilchenphysik, Leopold-Franzens-Universität Innsbruck, A-6020 Innsbruck, Austria
[55] Department of Physics and Center for Space Sciences and Technology, University of Maryland Baltimore County, Baltimore, MD 21250, USA
[56] Department of Physics, Faculty of Science, Mahidol University, Bangkok 10400, Thailand
[57] Hiroshima Astrophysical Science Center, Hiroshima University, Higashi-Hiroshima, Hiroshima 739-8526, Japan
[58] Laboratoire Univers et Particules de Montpellier, Université Montpellier, CNRS/IN2P3, F-34095 Montpellier, France
[59] Istituto Nazionale di Fisica Nucleare, Sezione di Trieste, and Università di Trieste, I-34127 Trieste, Italy
[60] Department of Physics and Astronomy, University of Denver, Denver, CO 80208, USA
[61] Osservatorio Astronomico di Trieste, Istituto Nazionale di Astrofisica, I-34143 Trieste, Italy
[62] Department of Physics and Astronomy, University of Padova, Vicolo Osservatorio 3, I-35122 Padova, Italy
[63] Korea Astronomy and Space Science Institute, 776 Daedeokdae-ro, Yuseong-gu, Daejeon 30455, Republic of Korea
[64] Department of Physics, American University, Washington, DC 20016, USA
[65] Centre for Astro-Particle Physics (CAPP) and Department of Physics, University of Johannesburg, PO Box 524, Auckland Park 2006, South Africa
[66] Santa Cruz Institute for Particle Physics, Department of Physics and Department of Astronomy and Astrophysics, University of California at Santa Cruz, Santa Cruz, CA 95064, USA
[67] Department of Physics, The University of Hong Kong, Pokfulam Road, Hong Kong, People's Republic of China
[68] Laboratory for Space Research, The University of Hong Kong, Hong Kong, People's Republic of China
[69] NYCB Real-Time Computing Inc., Lattingtown, NY 11560-1025, USA
[70] Purdue University Northwest, Hammond, IN 46323, USA
[71] Solar-Terrestrial Environment Laboratory, Nagoya University, Nagoya 464-8601, Japan
[72] Department of Physics, University of Maryland, College Park, MD 20742, USA
[73] Institute of Space Sciences (ICE, CSIC), Campus UAB, Carrer de Magrans s/n, E-08193 Barcelona, Spain; and Institut d'Estudis Espacials de Catalunya (IEEC), E-08034 Barcelona, Spain
[74] Institució Catalana de Recerca i Estudis Avançats (ICREA), E-08010 Barcelona, Spain
[75] Praxis Inc., Alexandria, VA 22303, resident at Naval Research Laboratory, Washington, DC 20375, USA
[76] Center for Astrophysics and Cosmology, University of Nova Gorica, Nova Gorica, Slovenia
[77] School of Astronomy and Space Science, University of Science and Technology of China, Hefei 230026, People's Republic Of China
*Received 2022 January 28; revised 2022 April 12; accepted 2022 April 25; published 2022 July 14*

## Abstract

Cosmic rays are mostly composed of protons accelerated to relativistic speeds. When those protons encounter interstellar material, they produce neutral pions, which in turn decay into gamma-rays. This offers a compelling way to identify the acceleration sites of protons. A characteristic hadronic spectrum, with a low-energy break around 200 MeV, was detected in the gamma-ray spectra of four supernova remnants (SNRs), IC 443, W44, W49B, and W51C, with the Fermi Large Area Telescope. This detection provided direct evidence that cosmic-ray protons are (re-)accelerated in SNRs. Here, we present a comprehensive search for low-energy spectral breaks among 311 4FGL catalog sources located within 5° from the Galactic plane. Using 8 yr of data from the Fermi Large Area Telescope between 50 MeV and 1 GeV, we find and present the spectral characteristics of 56 sources with a spectral break confirmed by a thorough study of systematic uncertainty. Our population of sources includes 13 SNRs for which the proton–proton interaction is enhanced by the dense target material; the high-mass gamma-ray binary LS I+61 303; the colliding wind binary $\eta$ Carinae; and the Cygnus star-forming region. This analysis better constrains the origin of the gamma-ray emission and enlarges our view to potential new cosmic-ray acceleration sites.

*Unified Astronomy Thesaurus concepts:* Gamma-ray sources (633); Supernova remnants (1667)

*Supporting material:* machine-readable table

## 1. Introduction

The acceleration site of protons, the main component of cosmic rays, is one of the most fundamental topics of high-energy astrophysics. The strong shocks associated with supernova remnants (SNRs) are widely believed to accelerate the bulk of Galactic cosmic rays ($E < 10^{15}$ eV) through the diffusive shock acceleration mechanism (e.g., Drury 1983). Indeed, accelerated cosmic rays interact with surrounding matter and produce $\pi^0$ mesons, which usually quickly decay into two gamma-rays, each having an energy of 67.5 MeV in the rest frame of the neutral pion. In turn, the gamma-ray number spectrum $F(E)$ is symmetric at this same energy in log–log representation (Stecker 1971), which then leads to a gamma-ray spectrum in the usual $E^2F(E)$ representation rising below 200 MeV and approximately tracing the energy distribution of parent protons at energies greater than a few gigaelectronvolts. This characteristic spectral feature, often referred to as the *pion-decay bump*, uniquely identifies proton acceleration since leptonic gamma-ray production mechanisms

such as bremsstrahlung and inverse Compton (IC) emission require fine-tuning to produce a similar feature. Esposito et al. (1996) explored this hypothesis by studying the gamma-ray emission from SNRs, and potential associations of gamma-ray sources with five radio-bright shell-type SNRs were reported using data taken by the EGRET instrument onboard the Compton Gamma Ray Observatory. More recently, this signature of protons was detected in five SNRs interacting with molecular clouds (MCs) and detected at gamma-ray energies by Fermi-LAT: IC 443 and W44 (Giuliani et al. 2011; Ackermann et al. 2013), W49B (H.E.S.S. Collaboration et al. 2018a), W51C (Jogler & Funk 2016), and HB 21 (Ambrogi et al. 2019), although in this last source both the leptonic and hadronic processes are able to reproduce the gamma-ray emission. Finally, the young SNR Cassiopeia A was also analyzed at low energy and Yuan et al. (2013) derived an energy break at $1.72^{+1.35}_{-0.89}$ GeV, which is better reproduced by a hadronic scenario. More details on this characteristic feature observed in the gamma-ray emission are provided in Appendix A, showing a stronger signature for a soft proton injection index ($\Gamma = 2.5$) than for a hard index ($\Gamma = 1.5$).

Electrons can also radiate at gamma-ray energies via the IC scattering and bremsstrahlung processes. It has been demonstrated, for the SNRs interacting with the molecular clouds (MCs) cited above, that the large gamma-ray luminosity is difficult to explain via IC scattering. In addition, the steep gamma-ray spectrum detected at low energy requires additional breaks in the electron spectrum if we consider a model in which electron bremsstrahlung is dominant. Accurate estimation of the spectral characteristics of a gamma-ray source at low energy is therefore crucial since it probes the nature of the particles (electrons or protons) emitting these gamma-rays. However, the analysis of sources below 100 MeV is complicated due to large uncertainties in the arrival directions of the gamma-rays, which lead to confusion among point sources and difficulties in separating point sources from diffuse emission. Thus, catalogs released by the Fermi-LAT Collaboration have focused on energies greater than 100 MeV until the 4FGL catalog (Abdollahi et al. 2020) expanded the lower bound to 50 MeV. This allows better constraint of low-energy spectra, but since the 4FGL upper energy bound is 1 TeV, the spectral model for most sources is dominated by data with energies above a few hundred megaelectronvolts. In addition, the spectral representation of sources in the 4FGL catalog considered three spectral models: power law (PL), PL with sub-exponential cutoff, and log-normal (or log parabola, hereafter called LP). This means that any source presenting a spectral break will be represented by a log-normal shape that may not adequately represent the low-energy behavior. Similarly, sources presenting two spectral breaks, as is the case for W49B (H.E.S.S. Collaboration et al. 2018a) will be represented with a log-normal shape that better describes the high-energy interval due to the better angular resolution and increased effective area at these high energies. This directly implies that the description of the low-energy spectral parameters of a source requires a dedicated spectral analysis.

In this paper, we use 8 yr of Pass 8 data to analyze 311 Galactic sources detected in the 4FGL catalog and search for significant spectral breaks between 50 MeV and 1 GeV. The paper is organized as follows: Section 2 describes the LAT and the observations used, Section 3 presents our systematic methods for analyzing LAT sources in the plane at low energy, Section 4 discusses the main results and a summary is provided in Section 5.

## 2. Fermi-LAT Description and Observations

### 2.1. Fermi-LAT

Fermi-LAT is a gamma-ray telescope that detects photons with energies from 20 MeV to more than 500 GeV by conversion into electron-positron pairs, as described in Atwood et al. (2009). The LAT is composed of three primary detector subsystems: a high-resolution converter/tracker (for measurement of the direction of the incident gamma-rays), a CsI(Tl) crystal calorimeter (for energy measurement), and an anticoincidence detector to identify the background of charged particles. Since the launch of the spacecraft in 2008 June, the LAT event-level analysis has been upgraded several times to take advantage of the increasing knowledge of how Fermi-LAT functions as well as the environment in which it operates. Following the Pass 7 data set, released in 2011 August, Pass 8 is the latest version of Fermi-LAT data. Its development is the result of a long-term effort aimed at a comprehensive revision of the entire event-level analysis and comes closer to realizing the full scientific potential of the LAT (Atwood et al. 2013). The current version of LAT data is Pass 8 P8R3 (Atwood et al. 2013; Bruel et al. 2018). It offers 20% more acceptance than P7REP (Bregeon et al. 2013). We used the SOURCE class event selection, with the instrument response functions (IRFs) P8R3_SOURCE_V3.

### 2.2. Data Selection and Reduction

We used exactly the same data set as that used to derive the 4FGL catalog of sources, namely, 8 yr (2008 August 4–2016 August 2) of Pass 8 SOURCE class photons. This means that similarly to the 4FGL data set, our data were filtered removing time periods when the rocking angle was greater than 90° and intervals around solar flares and bright gamma-ray bursts (GRBs) were excised.

Pass 8 introduced a new partition of the events, called PSF event types, based on the quality of the angular reconstruction, with approximately equal effective area in each event type at all energies. Due to the very low signal-to-noise ratio at low energy, the angular resolution is critical to distinguish point sources from the background and we decided to use only PSF3 events (the best-quality events) below 100 MeV. We add PSF2 events between 100 MeV and 1 GeV. This high-energy bound was selected since middle-aged SNRs commonly exhibit a high-energy spectral break at around 1–10 GeV, which would then bias our low-energy analysis (Uchiyama et al. 2010). For both PSF3 and PSF2 events, we excised photons detected with zenith angles larger than 80° to limit the contamination from gamma-rays generated by cosmic-ray interactions in the upper layers of the atmosphere. That procedure eliminates the need for a specific Earth limb component in the model.

The data reduction and exposure calculations are performed using the LAT *fermitools* version 1.2.23 and *family* (Wood et al. 2017) v0.19.0. We used only binned likelihood analysis because the unbinned mode is much more CPU intensive and does not support energy dispersion.

We accounted for the effect of energy dispersion (reconstructed event energy not equal to the true energy of the incoming gamma-ray), which becomes significant at low energies (see below). To do so, we used edisp_bins = −3,

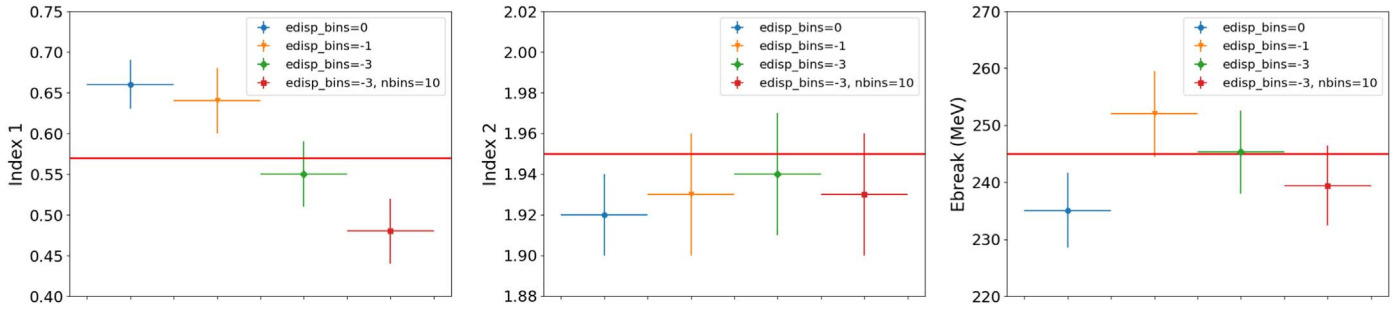


**Figure 1.** Effect of the number of energy bins and value of edisp_bins on the reconstructed values of the spectral index $\Gamma_1$ (left), $\Gamma_2$ (middle) and the break energy (right) of the broken PL model of IC 443. Four configurations are tested: 12 energy bins and edisp_bins = 0 (blue circle), 12 energy bins and edisp_bins = −1 (orange triangle), 12 energy bins and edisp_bins = −3 (green diamond), and 10 energy bins and edisp_bins = −3 (red square).

which means that the energy dispersion correction operates on the spectra with three extra bins below and above the threshold of the analysis.[78]

Our binned analysis includes three logarithmically spaced energy bins between 50 and 100 MeV, and 9 energy bins between 100 MeV and 1 GeV. The Galactic diffuse emission was modeled by the standard file gll_iem_v07.fits and the residual background and extragalactic radiation were described by an isotropic component (depending on the point-spread function (PSF) event type) with the spectral shape in the tabulated model iso_P8R3_SOURCE_V3_PSF(3/2)_v1.txt. The models are available from the Fermi Science Support Center.[79] In the following, we fit the normalizations of the Galactic diffuse and the isotropic components.

### 2.3. Effect of the Energy Dispersion

A crucial point that needs to be considered when analyzing LAT data at low energies is the effect of energy dispersion. For Pass 8, the energy resolution is < 10% between 1 and 100 GeV but it worsens below 1 GeV. It is ∼20% at 100 MeV and ∼28% at 30 MeV. The combination of energy dispersion and the rapidly changing effective area below 100 MeV could result in biased measurements of flux and spectral index of the source under study. In order to quantify the effects of energy dispersion, 200 simulations of the spectrum of IC 443 as published by Ackermann et al. (2013) were performed for an 8 yr observation time using the *gtobssim* tool included in the LAT *fermitools*. For these simulations, we assumed a point-source spatial model located at (R.A., decl. (J2000): 94°.51, 22°.66) and a smooth broken PL spectral model of the form:

$$\frac{dN}{dE} = N_0(E/E_0)^{-\Gamma_1}(1 + (E/E_{\rm br})^{(\Gamma_2-\Gamma_1)/\alpha})^{-\alpha}, \quad (1)$$

where $\alpha = 0.1$, the break energy $E_{\rm br} = 245$ MeV, and the spectral indices $\Gamma_1 = 0.57$, $\Gamma_2 = 1.95$. These simulations include the effect of energy dispersion. The analysis of these simulations was performed with the exact same configuration (region size, PSF components used, spatial bin size, energy interval) as the one used for real data. The only two parameters that have been varied in this study are the number of energy intervals and the value of the parameter edisp_bins as discussed in Section 2.2. For each combination of (energy bins, edisp_bins), we analyzed the 200 simulations, plotted the distributions of the reconstructed values of the break energy, $\Gamma_1$ and $\Gamma_2$, and fitted a Gaussian on each distribution.

The centroid of the Gaussian fit together with their size are reported in Figure 1 for the four tests performed: (12 energy bins, edisp_bins = 0), (12 energy bins, edisp_bins = −1), (12 energy bins, edisp_bins = −3), and (10 energy bins, edisp_bins = −3). As can be seen in this figure, the main effect is on $\Gamma_1$, as expected. If the energy dispersion is not taken into account (edisp_bins = 0), the spectrum falls less steeply at low energy and the spectral index $\Gamma_1$ is reconstructed with a value 0.1 higher than the simulated value set in the simulations. This is also true if the energy dispersion is taken into account with only one extra bin (edisp_bins = −1), which is not sufficient to properly take into account the effect of energy dispersion at these low energies even if this configuration has the advantage to reproduce slightly more accurately the value of the break energy. Even with a configuration using edisp_bins = −3, if the number of bins is too small, the reconstructed value of $\Gamma_1$ will be biased toward a lower value, which will artificially create a stronger break at low energy. This is directly due to the fact that the energy resolution varies with energy. This requires choosing an energy binning that is fine enough to capture this energy dependence. The best compromise that was found between good reconstruction and computation time (since higher values of edisp_bins or of the number of energy bins increase the CPU time) was obtained for a configuration using edisp_bins = −3 and 12 energy bins between 50 MeV and 1 GeV. This configuration was used for all results presented in the following.

## 3. Detection of Spectral Breaks

### 3.1. List of Candidates

This analysis intends to find new cosmic-ray acceleration sites in our Galaxy. When cosmic-ray protons accelerated by a source penetrate high-density clouds, the gamma-ray emission is expected to be enhanced relative to the interstellar medium because of the more frequent proton–proton interactions. Targeting the presence of such clouds, we restricted our search to sources within 5° from the Galactic plane. In addition, we removed from our list all identified pulsars and active galactic nuclei (AGNs). For AGNs, we removed all subclasses, namely, flat-spectrum radio quasars, BL Lac-type objects, blazar candidates of uncertain type, radio galaxies, narrow-line Seyfert 1, steep spectrum radio quasars, Seyfert galaxies, or simply AGNs. Finally, to ensure that the source is significant in the low-energy domain covered by our analysis, we removed all sources with a significance below 3$\sigma$ between 300 MeV and

[78] https://fermi.gsfc.nasa.gov/ssc/data/analysis/documentation/Pass8_edisp_usage.html
[79] http://fermi.gsfc.nasa.gov/ssc/

1 GeV as reported in the 4FGL catalog. In the end, these selection criteria provide us with the list of 311 candidates reported in Appendix B.

### 3.2. Input Source Model Construction

We perform an independent analysis of the 311 candidates selected in Section 3.1. The procedure followed is inspired by the Fermi High-Latitude Extended Sources Catalog (Ackermann et al. 2018), which already used the functions provided by *fermipy*.

For each source of interest, we define a $20^\circ \times 20^\circ$ region and include in our baseline model all 4FGL sources located in a $40^\circ \times 40^\circ$ region centered on our source of interest (SOI). We model each 4FGL source using the same spectral parameterization as used in the 4FGL. For extended sources, we use the spatial models from the 4FGL and keep them as fixed parameters since the angular resolution between 50 MeV and 1 GeV does not allow us to perform a morphological analysis. Similarly, the positions of all point sources are fixed at their 4FGL values.

Starting from the baseline model, we proceed to optimize the model using the optimize function provided by *fermipy*. In this optimization step, we first fit the spectral parameters of the Galactic interstellar emission model and residual background together with the normalization of the five brightest sources.

Then, we individually fit the normalizations of all sources inside the region of interest (ROI) that were not included in the first step in the order of their total predicted counts in the model (Npred) down to Npred = 1. The optimization is concluded by individually fitting the index and normalization parameters of all sources with a test statistic (TS) value above 25 starting from the highest TS sources. This TS value is determined from the first two steps of the ROI optimization by $\mathrm{TS} = 2(\ln \mathcal{L}_1 - \ln \mathcal{L}_0)$, where $\mathcal{L}_0$ and $\mathcal{L}_1$ are the likelihoods of the background (null hypothesis) and the hypothesis being tested (source plus background). This optimization is followed by a second one where the number of bright sources fit together with the diffuse backgrounds is increased to 10. This allows a better convergence for complex regions containing a large number of bright sources.

After optimizing the parameters of the baseline model components, we then perform a fit of the region by leaving free the normalization of all sources within $2^\circ$ of the SOI, their spectral shape if their TS value is above 16, the normalization of all sources with $\mathrm{TS} > 100$ in the ROI and the spectral shape of all sources in the ROI with $\mathrm{TS} > 200$. If the number of degrees of freedom (Ndof) is above 100, we increase the two last TS criteria by 100 until the Ndof becomes smaller than 100.

Once this complete fit of the ROI is performed, we further refine the model by identifying and adding new point-source candidates. We identify candidates by generating a TS map for a point source that has a PL spectrum with an index of $\Gamma = 2$. When generating the TS map, we fix the parameters of the background sources and fit only the amplitude of the test source. We add a source at every peak in the TS map with $\mathrm{TS} > 16$ that is at least $2^\circ$ from a peak with higher TS due to the poor angular resolution at these low energies. New source candidates are modeled with a PL whose normalization and index are fit in this procedure. We then generate a new TS map after adding the point sources to the model and repeat the procedure until no candidates with $\mathrm{TS} > 16$ are found. Though we do not expect to find a large number of additional sources, this step is crucial since we are not using the weights, first introduced for the 4FGL Catalog (Abdollahi et al. 2020). Indeed, the generation of the candidate list for the catalog is done above 100 MeV (instead of 50 MeV for our analysis) and each candidate is kept if the TS value obtained via a weighted maximum likelihood fit is above 25. These weights mitigate the effect of systematic errors due to our imperfect knowledge of the Galactic diffuse emission. As a consequence, the TS value of soft sources decreases.

In the final pass of the analysis, a second general fit of the ROI is performed using the same criteria as above to free the spectral parameters of all sources. If sources added previously by using the TS map fall below $\mathrm{TS} > 16$, they are removed from the model. If their TS value is above 16 and they are located at a distance smaller than $5^\circ$ from our SOI, we test iteratively for each of them the improvement of the log-normal representation with respect to the PL model. The LP model is defined as

$$\frac{dN}{dE} = N_0 \left(\frac{E}{E_0}\right)^{-(\alpha+\beta \log (E/E_0))}, \quad (2)$$

where $N_0$ is the overall normalization factor to scale the observed brightness of a source, $E_0$ is a fixed scale energy (kept at 300 MeV in our analysis), and $\alpha$, $\beta$ are left free, which adds 1 degree of freedom with respect to the PL representation. The improvement of the LP model with respect to the PL one is performed by determining $\mathrm{TS_{LP}} = 2(\ln \mathcal{L}_{\mathrm{LP}} - \ln \mathcal{L}_{\mathrm{PL}})$. If $\mathrm{TS_{LP}}$ is above 9 (which corresponds to a $3\sigma$ improvement for one additional degree of freedom), we switch to the log-normal representation. The spectral parameters of all added sources located within $5^\circ$ of a candidate are reported in Table 1. As can be seen, the curvature index $\beta$ is hard to constrain for the additional faint sources, even if the LP model significantly improves the fit. It is also clear that several added sources are located within the Vela and Cygnus regions for which the morphological templates used for the Vela-X PWN or the Cygnus Cocoon are not precise enough to properly characterize the region. Because the 4FGL Catalog rejects most point sources found inside extended sources, this leaves many residuals that translate into sources.

### 3.3. Spectral Energy Breaks

Once the ROI is well characterized, we first test the TS value of our SOI in our energy range (50 MeV−1 GeV). If it is below 25, we stop the analysis for this source since it is not significantly detected in our pipeline. It is the case for 64 sources among the 311 selected and their TS values are reported in Table B1. If the TS of the SOI is above 25, we move on and we fix all sources located more than $5^\circ$ from the SOI and we test the spectral curvature of our SOI.

To ensure that the curvature is real and affects several energy bins as would be the case for a pion-decay bump signature, we first test a log-normal representation for the source as defined in Equation (2). If $\mathrm{TS_{LP}}$ is below 9, we consider that no significant curvature is detected by our pipeline, we report this value in Table B1 and we stop the analysis of this source. This is the case for 167 sources in our sample.

If the value is above 9, we then test a smoothly broken PL following Equation (1), where $N_0$ is the differential flux at $E_0 = 300$ MeV and $\alpha = 0.1$, as was done previously for the

**Table 1**
Localization and TS Value of Added Sources Localized Within 5° of a Confirmed Candidate with a Significant Spectral Break (the Reference Energy $E_0$ is Fixed at 300 MeV in All Cases)

| Name | R.A., Decl. (°), (°) | TS Value | $TS_{LP}$ | Prefactor ($10^{-11}$ $cm^{-2}s^{-1}MeV^{-1}$) | Index | $\beta$ |
|---|---|---|---|---|---|---|
| PS J0216.4+6213 | 34.12, 62.23 | 31 | 1 | $2.1 \pm 0.6$ | $1.8 \pm 0.3$ | |
| PS J0327.6+5329 | 51.92, 53.49 | 30 | 5 | $1.0 \pm 0.3$ | $1.7 \pm 0.3$ | |
| PS J0533.7+2501 | 83.45, 25.03 | 72 | 3 | $0.8 \pm 0.2$ | $4.2 \pm 0.2$ | |
| PS J0845.8-4448 | 131.46, −44.81 | 30 | 4 | $3.0 \pm 0.7$ | $2.3 \pm 0.2$ | |
| PS J0838.1-4212 | 129.55, −42.21 | 66 | 16 | $5.2 \pm 0.9$ | $2.0 \pm 0.3$ | 1.0 |
| PS J0856.8-4245 | 134.21, −42.76 | 59 | 5 | $2.6 \pm 0.2$ | $1.9 \pm 0.1$ | |
| PS J0900.7-4438 | 135.20, −44.64 | 92 | 5 | $2.8 \pm 0.2$ | $1.5 \pm 0.1$ | |
| PS J1558.2-5029 | 239.56, −50.50 | 51 | 28 | $5.5 \pm 0.7$ | $2.7 \pm 0.2$ | 1.0 |
| PS J1603.6-4621 | 240.92, −46.35 | 35 | 10 | $2.5 \pm 0.4$ | $2.0 \pm 0.2$ | 1.0 |
| PS J1632.5-4221 | 248.14, −42.35 | 39 | 7 | $1.7 \pm 0.3$ | $1.9 \pm 0.1$ | |
| PS J1642.0-4802 | 250.50, −48.05 | 32 | 2 | $3.6 \pm 0.9$ | $2.2 \pm 0.2$ | |
| PS J1816.9-1619 | 274.23, −16.32 | 46 | 8 | $4.9 \pm 0.9$ | $1.8 \pm 0.2$ | |
| PS J2026.4+4004 | 306.62, 40.07 | 88 | 0 | $5.7 \pm 0.1$ | $1.8 \pm 0.2$ | |
| PS J2032.0+3935 | 308.02, 39.59 | 131 | 7 | $6.6 \pm 0.7$ | $1.9 \pm 0.1$ | |
| PS J2038.7+4114 | 309.70, 41.24 | 87 | 10 | $7.4 \pm 0.7$ | $1.8 \pm 0.2$ | $0.7 \pm 0.2$ |
| PS J2035.7+4242 | 308.94, 42.71 | 50 | 0 | $3.5 \pm 0.4$ | $1.7 \pm 0.1$ | |
| PS J2018.8+4112 | 304.70, 41.20 | 74 | 12 | $8.9 \pm 1.0$ | $3.0 \pm 0.2$ | $0.5 \pm 0.1$ |
| PS J2045.5+4205 | 311.38, 42.10 | 48 | 9 | $4.9 \pm 0.8$ | $2.0 \pm 0.3$ | 1.0 |
| PS J2045.9+5044 | 311.48, 50.74 | 32 | 4 | $2.5 \pm 0.5$ | $1.8 \pm 0.2$ | |
| PS J2047.9+4456 | 311.99, 44.94 | 47 | 6 | $2.4 \pm 0.4$ | $1.8 \pm 0.2$ | |

**Note.** Columns 2 and 3 provide the R.A., decl. of the added source, and its TS value. Column 4 provides the improvement of the log-normal representation with respect to the PL model $TS_{LP}$ as defined in Section 3.2. If $TS_{LP} > 9$, a log-normal representation is favored and the index provided in Column 5 corresponds to the spectral parameter $\alpha$ in Equation (2), while $\beta$ is indicated in Column 6 in such cases. No errors on $\beta$ are reported when it hits the boundary of 1.0.

cases of IC 443 and W44 (Ackermann et al. 2013). This adds two additional degrees of freedom with respect to the PL model (the break energy $E_{br}$ and a second spectral index $\Gamma_2$). The improvement with respect to the PL one is determined by $TS_{SBPL} = 2(\ln \mathcal{L}_{SBPL} - \ln \mathcal{L}_{PL})$. Since this test requires the addition of 2 degrees of freedom to the fit and diffusive shock acceleration predicts $\Gamma_2 \sim 2$, we also test the improvement of the smooth broken PL with the second index fixed at 2 with respect to the PL one $TS_{SBPL2} = 2(\ln \mathcal{L}_{SBPL2} - \ln \mathcal{L}_{PL})$. We require $TS_{SBPL} > 12$ or $TS_{SBPL2} > 9$ (implying a $3\sigma$ improvement for two and one additional degrees of freedom, respectively) to keep the source in the significant energy break list reported in Table 2. We switch to the SBPL parameterization for all sources detected in this list. This means that, when a source located within 5° shows a significant energy break, we re-optimize the ROI and we redo the whole process as illustrated in the flowchart in Figure 2. This procedure allowed the detection of 77 sources presenting a significant energy break in their low-energy spectrum. The values of $TS_{LP}$, $TS_{SBPL}$, and $TS_{SBPL2}$ for each of them are reported in Table B1.

### 3.4. Diffuse and IRF Systematics

The primary source of systematic error in this low-energy analysis is the Galactic interstellar emission model (IEM). Our nominal Galactic IEM is the recommended one for PASS 8 source analysis. It represents the first major update to the LAT Collaboration's IEM since the model for the 3FGL catalog analysis gll_iem_v05.fits, developed for Pass 7 Source class, and later rescaled for Pass 8 Source as gll_iem_v06.fits. The development of the new model is described in more detail (including illustrations of the templates and residuals) online.[80]

[80] https://fermi.gsfc.nasa.gov/ssc/data/analysis/software/aux/4fgl/Galactic_Diffuse_Emission_Model_for_the_4FGL_Catalog_Analysis.pdf

The new model has higher resolution and correspondingly greater contrast but some shortcomings in the new Galactic IEM have been recognized when producing the 4FGL catalog.

To quantify the impact of diffuse systematics, we repeated our analysis for the 77 sources listed in Table 2 using the old diffuse rescaled for Pass 8 Source gll_iem_v06.fits. This alternative analysis means that the whole flowchart in Figure 2 was performed again, from the optimization of the ROI to the source finding algorithm, up to the determination of the spectral curvature. Performing the same complete analysis with the eight alternate diffuse models from Acero et al. (2016) would have become extremely CPU time-consuming and this is why the old diffuse model is only tested. Here, since we already know that the source presents a break with the new model, we directly tested if $TS_{SBPL} > 12$ or $TS_{SBPL2} > 9$. If it was not the case, then this source was discarded from the final list of sources presenting significant energy break.

The second source of systematic error in our analysis is the instrument response functions (IRFs) and especially the inaccuracies in the effective area. Following the standard method (Ackermann et al. 2012), we estimated the systematic error associated with the effective area by calculating uncertainties in the IRFs, which symmetrically bracket the standard effective area and flip from one extremum to the other at the measured value of the break energy. Here we started from the best-fit model obtained with the standard IRF, which is optimized before running the final spectral fit of each candidate with each of the two bracketing IRFs. The source finding algorithm was not relaunched in this case since these changes mainly affect the spectral parameters of the source and will not produce extra sources in the field of view.

A third source of systematic error that can affect the presence or absence of a spectral break for the SOI is related to the inaccuracy of the emission models of nearby point sources.

**Table 2**
Results of the Systematic Studies

| 4FGL Name | $TS_{SBPL}$ diffuse | $TS_{SBPL2}$ diffuse | $TS_{SBPL}$ Aeff min | $TS_{SBPL2}$ Aeff min | $TS_{SBPL}$ Aeff max | $TS_{SBPL2}$ Aeff max |
|---|---|---|---|---|---|---|
| ⋆4FGL J0222.4+6156e | 24.3 | 16.5 | 34.9 | 27.5 | 35.1 | 27.7 |
| ⋆4FGL J0240.5+6113 | 170.7 | 143.5 | 127.5 | 123.9 | 124.0 | 123.2 |
| ⋆4FGL J0330.7+5845 | 13.8 | 7.7 | 15.8 | 12.5 | 16.0 | 12.5 |
| ⋆4FGL J0340.4+5302 | 81.6 | 67.5 | 147.0 | 143.5 | 140.1 | 138.5 |
| ⋆4FGL J0426.5+5434 | 13.0 | 6.9 | 26.3 | 21.0 | 25.6 | 20.4 |
| ⋆4FGL J0500.3+4639e | 12.2 | 8.1 | 15.2 | 14.5 | 14.9 | 14.2 |
| ⋆4FGL J0540.3+2756e | 12.7 | 8.0 | 10.8 | 10.6 | 10.7 | 10.6 |
| ⋆4FGL J0609.0+2006 | 14.7 | 6.6 | 17.6 | 14.0 | 17.1 | 14.1 |
| ⋆4FGL J0617.2+2234e | 103.7 | 81.1 | 96.5 | 79.3 | 95.2 | 79.5 |
| 4FGL J0618.7+1211 | 10.4 | 5.7 | 16.5 | 9.3 | 15.2 | 9.5 |
| ⋆4FGL J0620.4+1445 | 13.5 | 6.0 | 14.0 | 9.2 | 14.2 | 9.3 |
| ⋆4FGL J0634.2+0436e | 26.3 | 21.3 | 17.6 | 17.6 | 10.5 | 10.6 |
| ⋆4FGL J0639.4+0655e | 33.3 | 28.9 | 44.8 | 39.3 | 45.0 | 39.4 |
| ⋆4FGL J0709.1-1034 | 26.5 | 14.6 | 19.5 | 13.0 | 19.4 | 13.0 |
| 4FGL J0722.7-2309 | 11.1 | 5.5 | 21.5 | 10.6 | 21.6 | 10.7 |
| 4FGL J0731.5-1910 | 9.4 | 5.1 | 16.4 | 9.4 | 16.3 | 9.4 |
| ⋆4FGL J0844.1-4330 | 27.1 | 13.2 | 38.9 | 13.2 | 32.7 | 11.2 |
| ⋆4FGL J0850.8-4239 | 15.2 | 9.0 | 27.4 | 19.7 | 27.7 | 19.9 |
| ⋆4FGL J0904.7-4908c | 15.8 | 9.4 | 11.8 | 9.7 | 12.5 | 10.0 |
| 4FGL J0911.6-4738 | 11.8 | 7.1 | 11.8 | 9.7 | 10.8 | 8.2 |
| 4FGL J0924.1-5202 | 11.9 | 6.6 | 16.8 | 9.2 | 18.5 | 9.3 |
| ⋆4FGL J1008.1-5706c | 21.5 | 9.9 | 25.7 | 20.6 | 25.7 | 20.8 |
| ⋆4FGL J1018.9-5856 | 14.7 | 5.2 | 28.9 | 27.9 | 28.5 | 28.2 |
| ⋆4FGL J1045.1-5940 | 25.6 | 19.8 | 15.2 | 15.0 | 17.0 | 16.9 |
| 4FGL J1244.3-6233 | 11.4 | 8.0 | 30.9 | 10.8 | 31.2 | 11.1 |
| ⋆4FGL J1351.6-6142 | 13.6 | 5.7 | 15.7 | 14.1 | 17.9 | 16.2 |
| ⋆4FGL J1358.3-6026 | 21.7 | 6.1 | 22.1 | 12.8 | 22.5 | 13.1 |
| ⋆4FGL J1405.1-6119 | 23.6 | 16.2 | 25.1 | 20.1 | 25.1 | 20.1 |
| 4FGL J1408.9-5845 | 10.3 | 5.4 | 11.5 | 9.0 | 11.9 | 9.1 |
| ⋆4FGL J1442.2-6005 | 15.1 | 6.5 | 16.3 | 12.0 | 16.6 | 12.2 |
| ⋆4FGL J1447.4-5757 | 15.4 | 7.7 | 18.1 | 14.4 | 18.3 | 14.6 |
| 4FGL J1501.0-6310e | 7.9 | 3.2 | 17.8 | 10.0 | 18.4 | 10.1 |
| ⋆4FGL J1514.2-5909e | 14.0 | 11.3 | 34.1 | 27.8 | 32.9 | 29.1 |
| ⋆4FGL J1534.0-5232 | 12.2 | 5.3 | 13.6 | 8.5 | 13.9 | 8.4 |
| ⋆4FGL J1547.5-5130 | 17.0 | 12.9 | 32.8 | 16.3 | 30.8 | 18.3 |
| ⋆4FGL J1552.9-5607e | 12.0 | 7.9 | 11.5 | 10.9 | 11.9 | 10.9 |
| 4FGL J1553.8-5325e | 7.9 | 4.1 | 73.5 | 63.2 | 74.0 | 64.6 |
| 4FGL J1556.0-4713 | 9.8 | 5.8 | 11.4 | 4.8 | 10.2 | 4.6 |
| ⋆4FGL J1601.3-5224 | 34.2 | 21.9 | 42.9 | 36.9 | 44.6 | 36.5 |
| ⋆4FGL J1608.8-4803 | 20.4 | 13.7 | 30.8 | 13.2 | 30.7 | 13.4 |
| ⋆4FGL J1626.6-4251 | 20.8 | 13.9 | 18.2 | 8.7 | 15.2 | 8.8 |
| ⋆4FGL J1633.0-4746e | 12.8 | 8.5 | 37.2 | 36.4 | 38.1 | 37.1 |
| 4FGL J1639.3-5146 | 7.2 | 4.0 | 17.2 | 6.4 | 18.1 | 7.1 |
| 4FGL J1645.8-4533 | 8.9 | 6.6 | 28.9 | 10.5 | 30.9 | 14.6 |
| 4FGL J1708.6-4312 | 10.4 | 6.8 | 19.6 | 9.2 | 19.9 | 9.4 |
| 4FGL J1730.1-3422 | 9.8 | 1.5 | 35.6 | 13.8 | 35.9 | 14.1 |
| 4FGL J1734.5-2818 | 8.7 | 4.0 | 29.9 | 14.7 | 35.9 | 14.1 |
| ⋆4FGL J1742.8-2246 | 18.3 | 6.8 | 15.2 | 8.4 | 19.5 | 10.1 |
| 4FGL J1743.4-2406 | 7.0 | 3.8 | 14.7 | 5.3 | 14.9 | 6.5 |
| 4FGL J1759.7-2141 | 10.2 | 6.0 | 17.7 | 6.9 | 18.0 | 7.1 |
| ⋆4FGL J1801.3-2326e | 89.1 | 83.5 | 173.9 | 146.6 | 175.5 | 147.6 |
| ⋆4FGL J1808.2-1055 | 13.3 | 7.9 | 14.6 | 10.0 | 14.6 | 10.1 |
| ⋆4FGL J1812.2-0856 | 13.8 | 7.4 | 15.8 | 7.8 | 16.0 | 13.6 |
| ⋆4FGL J1813.1-1737e | 17.7 | 12.9 | 25.0 | 18.4 | 27.5 | 14.9 |
| ⋆4FGL J1814.2-1012 | 17.7 | 7.8 | 20.2 | 11.1 | 17.4 | 11.0 |
| ⋆4FGL J1839.4-0553 | 14.0 | 9.7 | 22.2 | 20.4 | 22.6 | 20.9 |
| ⋆4FGL J1852.4+0037e | 14.1 | 4.5 | 20.3 | 19.4 | 22.1 | 19.9 |
| ⋆4FGL J1855.2+0456 | 20.8 | 9.7 | 31.7 | 12.2 | 31.9 | 12.0 |
| ⋆4FGL J1855.9+0121e | 90.0 | 82.3 | 91.1 | 91.5 | 94.3 | 94.8 |
| 4FGL J1856.2+0749 | 8.5 | 4.5 | 21.1 | 19.5 | 19.3 | 14.8 |
| ⋆4FGL J1857.7+0246e | 12.0 | 5.6 | 24.4 | 20.5 | 24.9 | 19.1 |
| ⋆4FGL J1906.9+0712 | 11.3 | 10.9 | 28.1 | 18.7 | 28.0 | 19.8 |
| ⋆4FGL J1908.7+0812 | 15.8 | 10.3 | 62.3 | 41.8 | 62.9 | 42.1 |

**Table 2**
(Continued)

| 4FGL Name | $TS_{SBPL}$ diffuse | $TS_{SBPL2}$ diffuse | $TS_{SBPL}$ Aeff min | $TS_{SBPL2}$ Aeff min | $TS_{SBPL}$ Aeff max | $TS_{SBPL2}$ Aeff max |
|---|---|---|---|---|---|---|
| ⋆4FGL J1911.0+0905 | 14.4 | 10.4 | 27.8 | 27.6 | 27.8 | 27.4 |
| 4FGL J1912.5+1320 | 7.9 | 4.0 | 21.2 | 14.0 | 21.8 | 14.1 |
| ⋆4FGL J1923.2+1408e | 23.0 | 17.7 | 20.8 | 20.7 | 22.3 | 22.1 |
| ⋆4FGL J1931.1+1656 | 13.5 | 7.0 | 23.1 | 17.0 | 23.3 | 17.3 |
| ⋆4FGL J1934.3+1859 | 28.4 | 12.5 | 31.1 | 15.6 | 30.5 | 14.5 |
| 4FGL J1952.8+2924 | 8.0 | 4.0 | 20.6 | 12.4 | 21.0 | 12.6 |
| 4FGL J2002.3+3246 | 8.3 | 4.1 | 14.3 | 11.2 | 14.3 | 10.4 |
| ⋆4FGL J2021.0+4031e | 31.6 | 14.6 | 25.6 | 10.2 | 25.8 | 10.2 |
| ⋆4FGL J2028.6+4110e | 49.2 | 34.3 | 94.5 | 91.8 | 132.9 | 129.9 |
| ⋆4FGL J2032.6+4053 | 13.6 | 15.2 | 21.3 | 19.0 | 22.2 | 19.2 |
| ⋆4FGL J2038.4+4212 | 17.0 | 9.4 | 14.4 | 10.3 | 14.5 | 10.3 |
| ⋆4FGL J2045.2+5026e | 24.6 | 15.4 | 37.4 | 25.7 | 37.3 | 26.0 |
| ⋆4FGL J2056.4+4351c | 17.2 | 11.0 | 18.9 | 10.0 | 18.1 | 10.2 |
| ⋆4FGL J2108.0+5155 | 13.5 | 7.1 | 18.2 | 12.3 | 18.3 | 12.4 |

**Note.** Columns 2 and 3 are obtained with the Galactic diffuse background rescaled for Pass 8 Source (gll_iem_v06.fits) and provide values of the improvement of the smooth broken PL representation with respect to the PL model $TS_{SBPL}$ and the improvement of the smooth broken PL representation when fixing $\Gamma_2 = 2$ called $TS_{SBPL2}$ as defined in Section 3.2. Columns 4, 5, 6, and 7 provide the same values of $TS_{SBPL}$ and $TS_{SBPL2}$ for the two bracketing IRFs. Stars ⋆ denote spectral breaks that are robust to all tests. See Section 3.4 for more details.

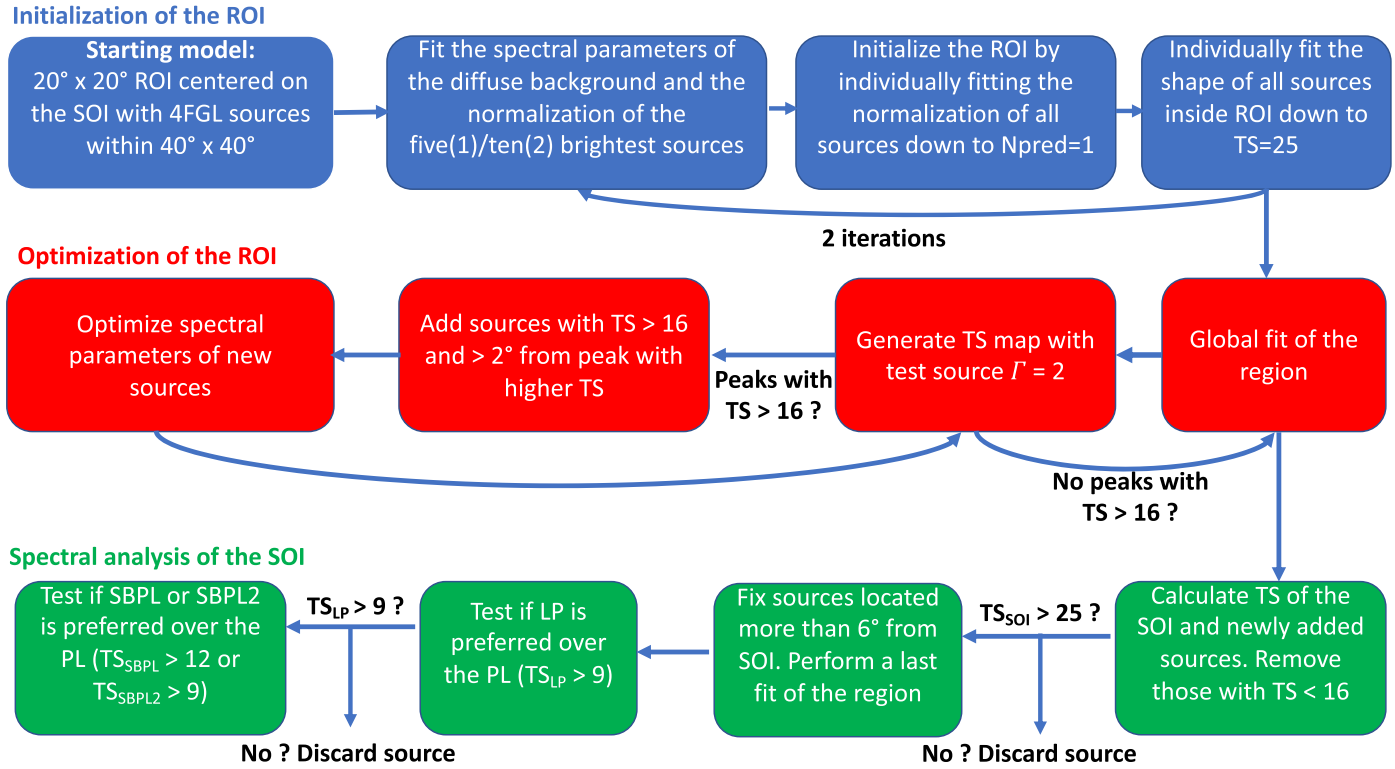


**Figure 2.** Flowchart illustrating the individual analysis procedure of each SOI located in a 20° × 20° region of interest. See text for further details.

A thorough investigation of this effect is beyond the scope of this paper but we included in Table 3, for each candidate, the distance of the nearest source as well as the relative contribution of photons from the neighboring sources and the diffuse backgrounds. Those values show that the diffuse background impacts the sources much more than their neighbors, with the exception of 4FGL J2021.0+4031e around the bright PSR J2021+4026.

Overall, 56 sources among the 77 sources detected with the standard IEM and IRFs are confirmed by our systematic studies. The 21 candidates rejected are all sources that do not meet the $TS_{SBPL}$ or $TS_{SBPL2}$ criteria when using the old diffuse model, while the inaccuracy in the effective area has a minor effect in our analysis as can be seen in Table 2. The spectral parameters of the confirmed sources are listed in Table 4. As can be seen in this table, even if the old diffuse background detects a significant energy break, the energy of this break can be significantly different than with the standard IEM, leading to large systematics as well on $\Gamma_1$. However, the value of $\Gamma_2$ is much more robust.

**Table 3**
Fractions of Photons from Neighboring Sources and Diffuse Background Affecting All Confirmed Sources Showing a Significant Break

| 4FGL Name | Distance (°) | $N_{SOI}/N_{diff}$ | $N_{SOI}/N_{srcs}$ |
|---|---|---|---|
| 4FGL J0222.4+6156e | 0.76 | 0.85 | 3.61 |
| 4FGL J0240.5+6113 | 1.28 | 7.34 | 112.58 |
| 4FGL J0330.7+5845 | 2.51 | 0.14 | 22.24 |
| 4FGL J0340.4+5302 | 1.39 | 0.86 | 38.35 |
| 4FGL J0426.5+5434 | 0.99 | 0.68 | 311.20 |
| 4FGL J0500.3+4639e | 1.31 | 0.17 | 7.70 |
| 4FGL J0540.3+2756e | 1.35 | 0.08 | 1.99 |
| 4FGL J0609.0+2006 | 0.48 | 0.20 | 1.78 |
| 4FGL J0617.2+2234e | 0.40 | 5.40 | 28.79 |
| 4FGL J0620.4+1445 | 1.03 | 0.16 | 1.56 |
| 4FGL J0634.2+0436e | 1.29 | 0.22 | 2.74 |
| 4FGL J0639.4+0655e | 1.47 | 0.09 | 0.85 |
| 4FGL J0709.1-1034 | 1.42 | 0.25 | 10.44 |
| 4FGL J0844.1-4330 | 0.85 | 0.25 | 0.22 |
| 4FGL J0850.8-4239 | 0.68 | 0.29 | 0.80 |
| 4FGL J0904.7-4908c | 0.66 | 0.18 | 1.60 |
| 4FGL J1008.1-5706c | 0.59 | 0.19 | 2.76 |
| 4FGL J1018.9-5856 | 0.33 | 2.28 | 3.39 |
| 4FGL J1045.1-5940 | 0.52 | 1.39 | 2.76 |
| 4FGL J1351.6-6142 | 0.72 | 0.25 | 1.78 |
| 4FGL J1358.3-6026 | 0.48 | 0.27 | 1.32 |
| 4FGL J1405.1-6119 | 0.48 | 0.51 | 1.51 |
| 4FGL J1442.2-6005 | 0.24 | 0.17 | 0.95 |
| 4FGL J1447.4-5757 | 1.28 | 0.28 | 2.97 |
| 4FGL J1514.2-5909e | 0.69 | 0.24 | 1.06 |
| 4FGL J1534.0-5232 | 1.23 | 0.12 | 2.98 |
| 4FGL J1547.5-5130 | 0.66 | 0.17 | 2.28 |
| 4FGL J1552.9-5607e | 2.25 | 0.15 | 6.69 |
| 4FGL J1601.3-5224 | 1.46 | 0.14 | 3.64 |
| 4FGL J1608.8-4803 | 1.30 | 0.15 | 1.92 |
| 4FGL J1626.6-4251 | 0.75 | 0.12 | 1.33 |
| 4FGL J1633.0-4746e | 0.28 | 0.32 | 2.44 |
| 4FGL J1742.8-2246 | 1.00 | 0.20 | 1.22 |
| 4FGL J1801.3-2326e | 0.08 | 0.70 | 2.83 |
| 4FGL J1808.2-1055 | 1.14 | 0.17 | 1.38 |
| 4FGL J1812.2-0856 | 1.36 | 0.21 | 3.33 |
| 4FGL J1813.1-1737e | 0.50 | 0.20 | 2.43 |
| 4FGL J1814.2-1012 | 1.29 | 0.16 | 1.20 |
| 4FGL J1839.4-0553 | 0.28 | 0.45 | 0.87 |
| 4FGL J1852.4+0037e | 0.76 | 0.15 | 0.87 |
| 4FGL J1855.2+0456 | 1.25 | 0.16 | 2.01 |
| 4FGL J1855.9+0121e | 0.44 | 1.25 | 5.17 |
| 4FGL J1857.7+0246e | 0.45 | 0.22 | 1.34 |
| 4FGL J1906.9+0712 | 0.23 | 0.26 | 0.65 |
| 4FGL J1908.7+0812 | 0.94 | 0.20 | 1.54 |
| 4FGL J1911.0+0905 | 0.21 | 0.49 | 2.81 |
| 4FGL J1923.2+1408e | 0.35 | 0.91 | 3.27 |
| 4FGL J1931.1+1656 | 0.74 | 0.22 | 1.92 |
| 4FGL J1934.3+1859 | 0.55 | 0.21 | 0.72 |
| 4FGL J2021.0+4031e | 0.12 | 0.79 | 0.19 |
| 4FGL J2028.6+4110e | 0.73 | 0.16 | 0.43 |
| 4FGL J2032.6+4053 | 0.57 | 0.22 | 0.46 |
| 4FGL J2038.4+4212 | 0.71 | 0.24 | 1.09 |
| 4FGL J2045.2+5026e | 0.32 | 0.32 | 1.77 |
| 4FGL J2056.4+4351c | 1.07 | 0.18 | 3.63 |
| 4FGL J2108.0+5155 | 1.14 | 0.19 | 15.44 |

**Note.** Column 1 indicates the distance (in degrees) of the nearest neighboring source. Columns 2 and 3 list the ratio, in the pixel at the source position, between the predicted number of photons from the SOI with respect to those of the Galactic and isotropic diffuse background ($N_{SOI}/N_{diff}$), and to those of all neighboring sources $N_{SOI}/N_{srcs}$, respectively.

In addition to performing a spectral fit over the entire energy range, we computed an SED by fitting the flux of the source independently in 10 energy bins spaced uniformly in log space from 50 MeV–1 GeV. During this fit, we fixed the spectral index of the source at 2 as well as the model of background sources to the best fit obtained in the whole energy range except the normalizations of the Galactic diffuse and isotropic backgrounds. We determined the flux in an energy bin when $TS \geqslant 1$ and otherwise computed a 95% confidence level Bayesian flux upper limit, assuming a uniform prior on flux following Helene (1983). The systematic studies with the old diffuse and bracketing IRFs were also computed on all spectral energy distribution (SED) points for the 56 confirmed sources and the two uncertainties were added in quadrature. When an upper limit was derived, the maximal and minimal upper limits derived in this energy interval are plotted to indicate the systematics related to this data point.

## 4. Discussion

### 4.1. Population Study

We detected 56 4FGL gamma-ray sources showing a significant energy break in their spectrum between 50 MeV and 1 GeV confirmed by our studies of systematics. As can be seen in Figure 3, the distribution of sources showing a significant break in their low-energy spectrum is more uniform in both latitude and longitude than the parent distribution even if there remains a peak at latitude 0 and in the Galactic Ridge.

The sources that we detect significantly with our analysis ($TS > 25$) follow the same trend except for the region at $\sim 300°$ longitude, which contains more faint sources than the other regions of the plane. Figure 4 clearly shows that the sources that we do not detect with $TS > 25$ in our pipeline have predominantly low significance in the 4FGL catalog in the 300 MeV–1 GeV energy band, which is reassuring. However, there is no correlation between the significance value in the 4FGL catalog and the detection of a break with our pipeline. It can be seen in this same Figure since the distribution for the sources presenting a significant break is uniform.

The association summary is given in Table 5 and is illustrated by the pie charts in Figure 5. Out of 311 candidates, 210 are unidentified, representing 67.5% of the sources analyzed. It is striking to see that only 26 UNIDs show a spectral break confirmed by our systematic studies (which represents 46.4% of the sources with significant breaks). The 30 remaining candidates out of 56 confirmed cases present an association reported by the 4FGL Catalog listed in Table 6.

On the other hand, the fraction of sources associated with SNRs increases from 7.4% (23 out of 311 sources) to 23.2% (13 out of 56 sources). This makes SNRs the dominant class of sources with significant low-energy spectral break. Similarly, the fraction of sources associated with binaries increases from 1.6% (five out of 311) to 7.1% (four out of 56), showing that almost all binaries except 4FGL J1826.2-1450 (also known as LS 5039), show a significant spectral break. Despite their small fractions, binaries could contribute significantly to our population of sources with low-energy spectral breaks; however, it should be noted here that the spectral analysis is performed over 8 yr and these sources often present variable gamma-ray emission. A more thorough analysis of these sources would

**Table 4**
Spectral Parameters of All Confirmed Sources Showing a Significant Break

| 4FGL Name | I(50–1000) $10^{-6}$ (MeV cm$^2$ s$^{-1}$) | $\Delta I$(50–1000) stat/syst | $E_{\rm break}$ (MeV) | $\Delta E_{\rm break}$ stat/syst | $\Gamma_1$ | $\Delta\Gamma_1$ stat/syst | $\Gamma_2$ | $\Delta\Gamma_2$ stat/syst |
|---|---|---|---|---|---|---|---|---|
| 4FGL J0222.4+6156e | 47.8 | 2.7/0.6 | 465 | 78/40 | 1.35 | 0.14/0.03 | 2.34 | 0.21/0.14 |
| 4FGL J0240.5+6113 | 237.6 | 1.9/6.6 | 142 | 10/74 | 1.63 | 0.03/0.36 | 2.10 | 0.02/0.10 |
| 4FGL J0330.7+5845 | 3.2 | 0.5/0.3 | 367 | 38/52 | −0.68 | 0.75/0.81 | 3.42 | 0.64/0.21 |
| 4FGL J0340.4+5302 | 34.1 | 1.3/5.8 | 284 | 43/116 | 1.60 | 0.14/0.38 | 3.27 | 0.23/0.35 |
| 4FGL J0426.5+5434 | 15.1 | 0.8/0.9 | 338 | 47/80 | 1.25 | 0.16/0.35 | 2.50 | 0.18/0.07 |
| 4FGL J0500.3+4639e | 11.6 | 1.0/1.6 | 252 | 43/107 | 0.14 | 0.61/1.06 | 2.17 | 0.19/0.08 |
| 4FGL J0540.3+2756e | 14.8 | 1.5/4.8 | 493 | 82/146 | 0.90 | 0.25/0.54 | 2.64 | 0.52/0.37 |
| 4FGL J0609.0+2006 | 4.7 | 0.7/0.8 | 499 | 134/59 | 0.11 | 0.67/0.56 | 3.52 | 0.66/0.35 |
| 4FGL J0617.2+2234e | 122.5 | 2.4/1.1 | 276 | 19/3 | 1.06 | 0.05/0.03 | 1.75 | 0.03/0.03 |
| 4FGL J0620.4+1445 | 3.2 | 0.6/0.4 | 355 | 36/55 | 0.26 | 0.44/0.36 | 4.03 | 0.71/0.63 |
| 4FGL J0634.2+0436e | 24.1 | 1.4/15.5 | 243 | 41/121 | 1.07 | 0.13/0.50 | 2.00 | 0.13/0.26 |
| 4FGL J0639.4+0655e | 36.6 | 3.3/19.2 | 233 | 31/167 | −0.13 | 0.66/0.95 | 2.51 | 0.23/0.59 |
| 4FGL J0709.1-1034 | 5.1 | 0.8/2.2 | 351 | 57/23 | 0.06 | 0.90/0.25 | 3.40 | 0.56/0.36 |
| 4FGL J0844.1-4330 | 15.2 | 2.6/2.4 | 159 | 28/76 | 0.35 | 0.19/0.46 | 3.28 | 0.20/0.41 |
| 4FGL J0850.8-4239 | 10.8 | 1.4/1.7 | 424 | 83/26 | 1.24 | 0.12/0.11 | 3.71 | 0.30/0.03 |
| 4FGL J0904.7-4908c | 10.6 | 0.7/1.4 | 402 | 12/173 | 1.10 | 0.07/1.19 | 2.99 | 0.16/0.71 |
| 4FGL J1008.1-5706c | 12.3 | 1.6/5.1 | 409 | 76/37 | 0.96 | 0.43/0.55 | 3.40 | 0.64/0.33 |
| 4FGL J1018.9-5856 | 130.0 | 3.4/11.9 | 73 | 1/24 | 0.32 | 0.02/0.31 | 1.98 | 0.02/0.05 |
| 4FGL J1045.1-5940 | 49.8 | 2.3/6.0 | 525 | 26/178 | 1.12 | 0.05/0.17 | 2.12 | 0.11/0.14 |
| 4FGL J1351.6-6142 | 26.9 | 2.7/12.5 | 125 | 8/22 | −0.87 | 0.17/0.59 | 2.37 | 0.12/0.30 |
| 4FGL J1358.3-6026 | 20.8 | 1.5/2.3 | 131 | 4/28 | −0.63 | 0.05/0.52 | 2.55 | 0.07/0.13 |
| 4FGL J1405.1-6119 | 61.9 | 2.7/9.2 | 110 | 2/14 | 0.06 | 0.02/0.44 | 2.14 | 0.03/0.05 |
| 4FGL J1442.2-6005 | 21.3 | 1.7/6.9 | 126 | 2/21 | −1.10 | 0.03/0.73 | 2.58 | 0.07/0.44 |
| 4FGL J1447.4-5757 | 12.2 | 1.4/9.1 | 303 | 42/164 | 0.72 | 0.27/0.71 | 2.56 | 0.24/0.41 |
| 4FGL J1514.2-5909e | 38.4 | 3.2/10.4 | 116 | 9/27 | 1.08 | 0.10/0.69 | 2.92 | 0.10/0.05 |
| 4FGL J1534.0-5232 | 4.5 | 0.9/3.3 | 375 | 30/161 | 0.68 | 0.29/0.47 | 3.95 | 0.24/0.79 |
| 4FGL J1547.5-5130 | 12.8 | 2.8/1.1 | 349 | 331/47 | 1.31 | 0.09/0.49 | 4.68 | 0.14/0.18 |
| 4FGL J1552.9-5607e | 8.9 | 0.8/8.9 | 386 | 38/87 | 0.04 | 0.09/1.15 | 2.15 | 0.26/0.09 |
| 4FGL J1601.3-5224 | 26.1 | 2.4/3.2 | 356 | 23/177 | 1.19 | 0.17/0.77 | 3.78 | 0.32/0.89 |
| 4FGL J1608.8-4803 | 11.3 | 4.0/1.3 | 346 | 112/188 | 1.51 | 0.95/2.20 | 3.36 | 0.22/0.52 |
| 4FGL J1626.6-4251 | 4.5 | 0.7/1.0 | 354 | 16/32 | 0.63 | 0.31/0.28 | 4.57 | 0.15/0.58 |
| 4FGL J1633.0-4746e | 78.1 | 1.9/21.9 | 517 | 18/152 | 1.19 | 0.04/2.28 | 2.11 | 0.15/0.12 |
| 4FGL J1742.8-2246 | 5.7 | 0.7/0.8 | 364 | 22/44 | 0.28 | 0.17/0.32 | 3.40 | 0.15/0.30 |
| 4FGL J1801.3-2326e | 135.2 | 11.8/2.6 | 401 | 138/150 | 1.33 | 0.06/0.40 | 2.14 | 0.79/0.28 |
| 4FGL J1808.2-1055 | 3.5 | 1.4/1.9 | 354 | 6/39 | 0.22 | 0.51/0.67 | 2.81 | 0.75/0.31 |
| 4FGL J1812.2-0856 | 8.2 | 0.7/0.8 | 284 | 7/107 | 0.55 | 0.05/0.88 | 3.11 | 0.11/0.30 |
| 4FGL J1813.1-1737e | 56.0 | 3.1/12.4 | 154 | 3/84 | 0.22 | 0.41/0.25 | 2.17 | 0.03/0.42 |
| 4FGL J1814.2-1012 | 5.5 | 0.7/0.5 | 471 | 50/10 | 0.19 | 0.42/0.53 | 4.25 | 0.17/0.34 |
| 4FGL J1839.4-0553 | 62.4 | 3.8/8.4 | 86 | 3/30 | −0.29 | 0.33/0.30 | 1.94 | 0.04/0.10 |
| 4FGL J1852.4+0037e | 43.4 | 2.5/7.9 | 119 | 2/18 | −1.19 | 0.51/0.91 | 2.41 | 0.05/0.33 |
| 4FGL J1855.2+0456 | 13.5 | 3.1/0.1 | 379 | 157/56 | 0.53 | 0.12/0.44 | 3.76 | 0.25/0.44 |
| 4FGL J1855.9+0121e | 184.1 | 2.5/7.7 | 347 | 5/62 | 1.03 | 0.04/0.05 | 1.91 | 0.02/0.07 |
| 4FGL J1857.7+0246e | 37.7 | 0.8/17.7 | 615 | 20/284 | 1.51 | 0.04/1.58 | 2.45 | 0.12/0.24 |
| 4FGL J1906.9+0712 | 28.6 | 2.0/8.2 | 134 | 3/21 | −0.69 | 0.06/0.70 | 2.44 | 0.07/0.15 |
| 4FGL J1908.7+0812 | 30.6 | 1.1/17.5 | 137 | 3/170 | −1.19 | 0.05/1.54 | 2.75 | 0.08/0.88 |
| 4FGL J1911.0+0905 | 38.8 | 1.9/12.0 | 364 | 11/73 | 0.51 | 0.16/0.19 | 2.01 | 0.06/0.17 |
| 4FGL J1923.2+1408e | 93.6 | 2.1/3.9 | 381 | 14/131 | 1.39 | 0.01/0.51 | 2.11 | 0.04/0.11 |
| 4FGL J1931.1+1656 | 17.1 | 2.1/9.9 | 203 | 8/19 | −0.60 | 0.10/0.59 | 2.64 | 0.10/0.04 |
| 4FGL J1934.3+1859 | 15.9 | 2.0/3.5 | 211 | 23/11 | 0.17 | 0.38/0.23 | 3.13 | 0.27/0.12 |
| 4FGL J2021.0+4031e | 119.8 | 4.3/15.9 | 147 | 7/31 | 1.64 | 0.05/0.18 | 2.55 | 0.05/0.05 |
| 4FGL J2028.6+4110e | 201.5 | 5.2/77.9 | 383 | 13/138 | 1.00 | 0.02/0.37 | 2.23 | 0.06/0.24 |
| 4FGL J2032.6+4053 | 22.6 | 4.9/0.9 | 561 | 217/21 | 1.90 | 0.16/0.07 | 4.48 | 0.47/0.23 |
| 4FGL J2038.4+4212 | 20.2 | 2.0/4.3 | 152 | 22/187 | 0.65 | 0.23/0.29 | 2.29 | 0.14/0.31 |
| 4FGL J2045.2+5026e | 35.6 | 1.9/13.0 | 397 | 24/155 | 1.09 | 0.09/0.29 | 2.44 | 0.13/0.38 |
| 4FGL J2056.4+4351c | 9.0 | 1.1/5.2 | 183 | 5/65 | 0.02 | 0.04/0.29 | 2.52 | 0.07/0.22 |
| 4FGL J2108.0+5155 | 9.8 | 1.7/0.4 | 451 | 77/247 | 1.09 | 0.30/0.18 | 2.68 | 0.68/0.70 |

**Note.** Results of the maximum likelihood spectral fits for sources showing significant breaks confirmed by the systematic studies. These results are obtained using a smooth broken PL representation. Columns 2, 4, 6, and 8 list the integrated flux, the break energy and the photon indices $\Gamma_1$ and $\Gamma_2$ of the source fit in the energy range from 50 MeV–1 GeV following Equation (1). Columns 3, 5, 7, and 9 list the statistic and systematic uncertainties on these spectral parameters.

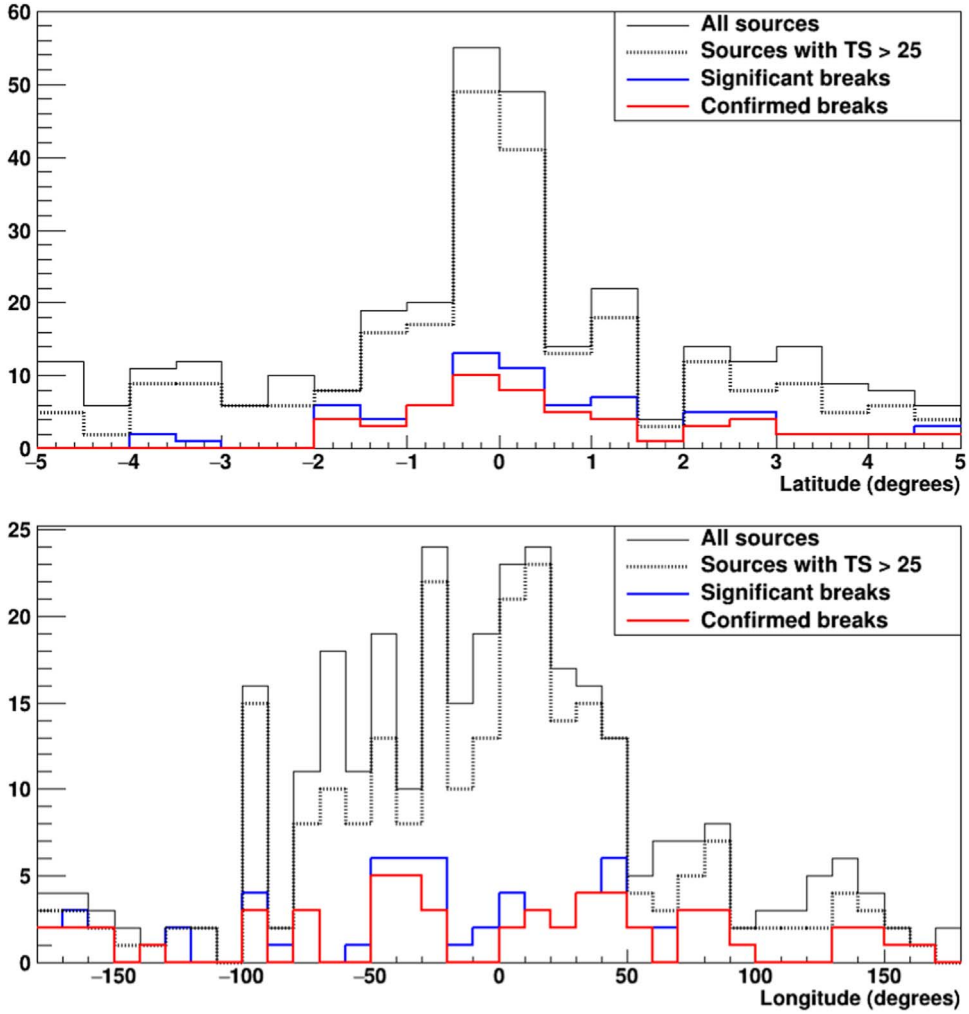


**Figure 3.** Latitude (top) and longitude (bottom) distributions of the 311 sources selected (black line), the 247 sources with TS $>$ 25 in our pipeline (black dashed line), the 77 sources with significant breaks (blue line) and the 56 confirmed cases by our studies of systematics (red line).

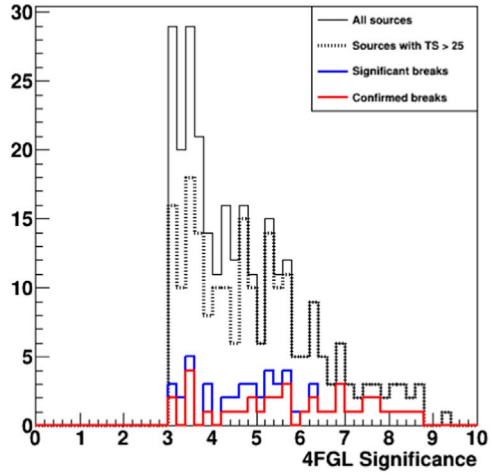


**Figure 4.** Distribution of the 4FGL significance between 300 MeV and 1 GeV for the 311 sources selected (black line), the 247 sources with TS $>$ 25 in our pipeline (black dashed line), the 77 sources with significant breaks (blue line) and the 56 confirmed cases by our studies of systematics (red line).

need to be done. Finally, only one SFR is analyzed (and confirmed) which prevents us from drawing a firm conclusion on this source class.

**Table 5**
Summary of Source Classes

| Source Class | Analyzed | Confirmed |
|---|---|---|
| Supernova remnant (SNR) | 23 | 13 |
| Pulsar wind nebulae (PWNe) | 4 | 2 |
| Supernova remnant/pulsar wind nebula (SPP) | 37 | 6 |
| Star-forming region (SFR) | 1 | 1 |
| Unknown (UNK) | 31 | 4 |
| Binary/high-mass binary (BIN/HMB) | 5 | 4 |
| Unidentified (UNID) | 210 | 26 |

**Note.** For the source classes SNR, PWNe, SPP, SFR, BIN, and HMB, we add both the firm identifications reported in the 4FGL catalog as well as the associations (capital and lower case letters as can be seen in Column 6 of Table B1).

Figure 6 illustrates the distribution over the sky of the 56 4FGL gamma-ray sources showing a significant energy SFR break. The lack of these sources at latitudes smaller than $-2°$ appears clearly. One can also note a large fraction of unidentified sources at longitude comprised between $-50°$ and $50°$. These sources are part of the large fraction of 4FGL unassociated sources located less than $10°$ away from the

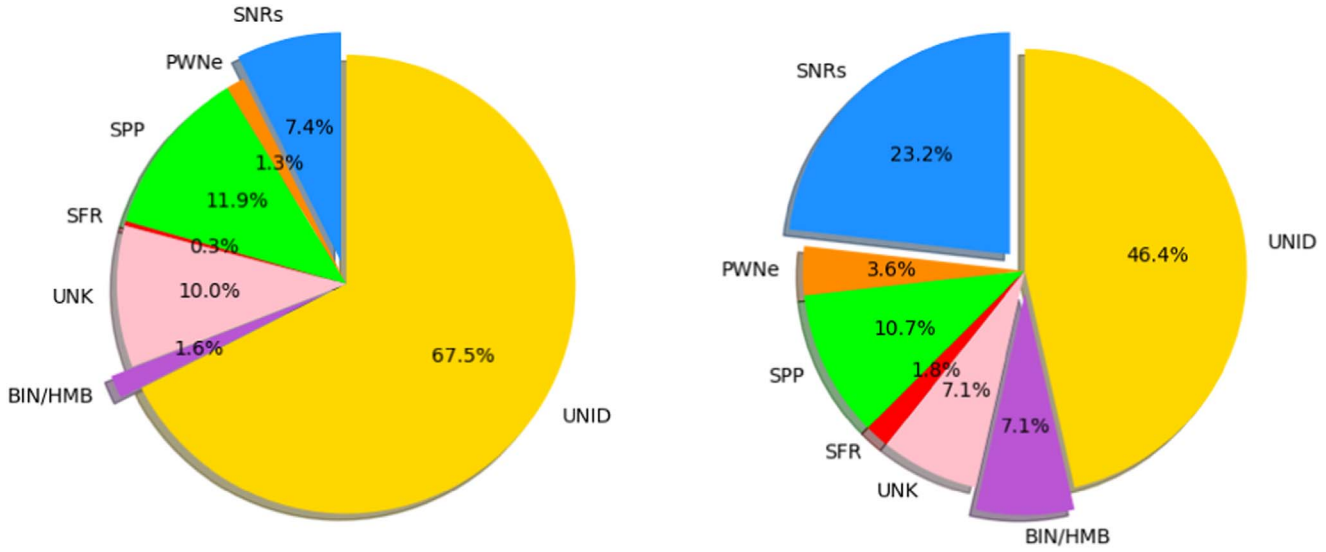


**Figure 5.** Pie charts showing the classes of sources analyzed (Left) and those for which a significant break is detected (Right). The class names are those used in the 4FGL catalog: SNR stands for supernova remnant, PWNe for pulsar wind nebulae, SFR for star-forming region, BIN for binary, HMB for high-mass binary. The designation SPP indicates potential association with SNR or PWNe. The UNK class includes low-latitude blazar candidates of uncertain type associated solely via the likelihood-ratio method.

**Table 6**
Candidates with Firm Associations Reported in the 4FGL Catalog

| 4FGL Name | Assoc1 | Assoc2 |
|---|---|---|
| 4FGL J0222.4+6156e | W3 | HB 3 field |
| 4FGL J0240.5+6113 | LS I+61 303 | |
| 4FGL J0500.3+4639e | HB 9 | |
| 4FGL J0540.3+2756e | Sim 147 | |
| 4FGL J0617.2+2234e | IC 443 | |
| 4FGL J0634.2+0436e | Rosette | Monoceros field |
| 4FGL J0639.4+0655e | Monoceros | |
| 4FGL J0904.7-4908 | 1RXS J090505.3-490324 | |
| 4FGL J1008.1-5706 | 1RXS J100718.2-570335 | |
| 4FGL J1018.9-5856 | 1FGL J1018.6-5856 | FGES J1036.3-5833 field |
| 4FGL J1045.1-5940 | Eta Carinae | FGES J1036.3-5833 field |
| 4FGL J1442.2-6005 | SNR G316.3-00.0 | |
| 4FGL J1514.2-5909e | MSH 15-52 | |
| 4FGL J1552.9-5607e | MSH 15-56 | |
| 4FGL J1601.3-5224 | SNR G329.7+00.4 | |
| 4FGL J1633.0-4746e | HESS J1632-478 | |
| 4FGL J1801.3-2326e | W28 | |
| 4FGL J1813.1-1737e | HESS J1813-178 | |
| 4FGL J1839.4-0553 | NVSS J183922-055321 | HESS J1841-055 field |
| 4FGL J1852.4+0037e | Kes 79 | |
| 4FGL J1855.9+0121e | W44 | |
| 4FGL J1857.7+0246e | HESS J1857+026 | |
| 4FGL J1911.0+0905 | W49B | |
| 4FGL J1923.2+1408e | W51C | |
| 4FGL J1934.3+1859 | SNR G054.4-00.3 | |
| 4FGL J2021.0+4031e | Gamma Cygni | Cygnus Cocoon field |
| 4FGL J2028.6+4110e | Cygnus X Cocoon | |
| 4FGL J2032.6+4053 | Cyg X−3 | Cygnus Cocoon field |
| 4FGL J2045.2+5026e | HB 21 | |
| 4FGL J2056.4+4351 | 1RXS J205549.4+435216 | |

**Note.** Columns 2 and 3 are derived from the Assoc1 and Assoc2 columns of the 4FGL Catalog. The latter provides an alternate designation or an indicator as to whether the source is inside an extended source.

Galactic plane with a wide latitude extension hard to reconcile with those of known classes of Galactic gamma-ray sources.

Looking now at the spectral parameters of the 56 confirmed sources, the distribution of the energy of the breaks detected by our analysis is relatively uniform between 70 and 700 MeV, with no breaks detected below and above this energy interval (as a direct consequence of the energy interval analyzed here) and a higher proportion of breaks at ∼400 MeV as illustrated

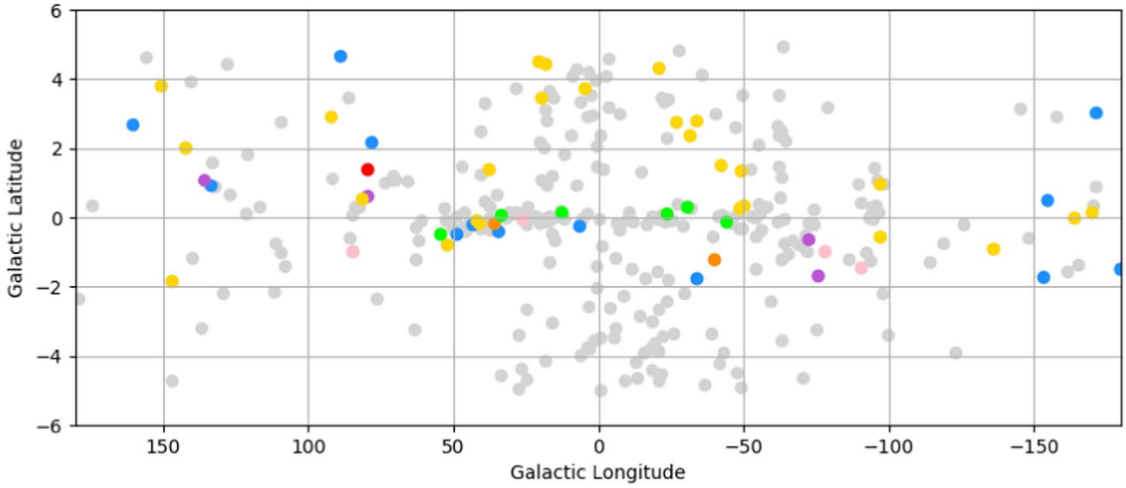


**Figure 6.** Distribution of sources in Galactic coordinates. Light gray markers indicate the 311 sources analyzed in this paper. Colored markers indicate the position of the 56 sources for which a significant break is detected: yellow for UNIDs, blue for SNRs, orange for PWNe, green for SPPs, red for SFR, pink for UNKs, and purple for BIN/HMB. The boundary of the latitude selection is 5°.

by Figure 7. Interestingly, no low-energy spectral breaks ($< 140$ MeV) are detected for the 13 sources associated with SNRs. As can be seen on the top panel of this figure, the large error bars on this parameter prevent us from drawing any firm conclusion or even rejecting any candidate by a comparison with the standard value expected for proton–proton interaction indicated by the green line. On the other hand, there is a trend concerning the distributions of $\Gamma_1$ with a peak at $\sim$0.2 and $\sim$1.0. The peak at 0.2 is expected by proton–proton interaction (as indicated by the green line presenting the results of the simulations carried out in Appendix A) but the peak at 1 is not predicted, though it is present for a large number of SNRs interacting with MCs. It might be due to some confusion by the Galactic and isotropic diffuse background. A double-peaked distribution is also visible in Figure 8 for $\Gamma_2$ at $\sim$2.1 and $\sim$3.6. For this parameter, the distribution restricted to SNRs contains a single peak at $\sim$2.1. Looking now at the distribution of $\Gamma_2 - \Gamma_1$ in Figure 8 (right), a peak at $\sim$0.9 is highly pronounced for SNRs. This tends to show that the values obtained on $\Gamma_2$ and $\Gamma_2 - \Gamma_1$ could be used in the future to probe the type of particles radiating in a gamma-ray source.

### 4.2. SNRs and MCs

The most famous sources with *pion bump* signature are the middle-aged remnants IC 443 and W44. Figure 9 presents the residual TS maps of the region of IC 443 (4FGL J0617.2+2234e) and W44 (4FGL J1855.9+0121e) as well as their SEDs, showing the overall agreement with the 4FGL SED points superimposed. This figure also illustrates the advantages of using a restricted energy range and different spectral shape than the 4FGL to better reproduce the significant energy break at low energy since we are not dominated here by photons at high energies. The spectral parameters reported in Table 4 for these two sources are in reasonable agreement with those published by Ackermann et al. (2013), knowing that this first analysis did not take into account the effect of energy dispersion and no systematic uncertainties were evaluated at that time.

Among the 56 sources with significant breaks, one can see from the 4FGL Classification column listed in Table B1 that 10 sources are firm SNR identifications and three are associated with SNRs. Among the three SNR associations, 4FGL J1911.0+0905 (Figure 17 top right) is associated with W49B and thus can be safely identified as an SNR since it is one of the few other sources for which a pion-decay bump signature was published with W51C (4FGL J1923.2+1408e, Figure 17, middle left) and HB 21 (4FGL J2045.2+5026e, Figure 18, middle right). The only missing source for which a low-energy break has been published is Cassiopeia A (4FGL J2323.4+5849) but the break energy reported by Yuan et al. (2013) is at $1.72^{+1.35}_{-0.89}$ GeV, which seems consistent with our non-detection in the 50 MeV–1 GeV energy interval. The five sources confirmed by our analysis are all SNRs interacting with MCs. These MCs are excellent targets for cosmic-ray interactions and subsequent pion decay.

The hadronic scenario was also preferred for other LAT-detected SNRs interacting with MCs, though their gamma-ray analysis starting above a few hundred megaelectronvolts did not allow rejection of a leptonic scenario: the SNR HB 3 and the W3 H II complex (Katagiri et al. 2016a), S147 (Katsuta et al. 2012), HB 9 (Araya 2014), the SNR G326.3-1.8 (Devin et al. 2018) and the SNR W28 (Hanabata et al. 2014). Our low-energy analysis presents a rapid turnover of the spectrum at low energy, which confirms the conclusions of the previous publications for 4FGL J0222.4+6156e (W3, see Figure 10, top left), 4FGL J0500.3+4639e (HB 9, see Figure 10, bottom right), 4FGL J0540.3+2756e (S147, Figure 11, top left) 4FGL J1552.9-5607e (G326.3-1.8, Figure 14, middle left) and 4FGL J1801.3-2326e (W28, see Figure 15, middle left). No significant curvature is detected for the SNR HB 3 but it should be noted that its gamma-ray emission is much fainter than the adjacent MC W3 (TS value of 75.9 with respect to 1307.1 for W3) and more data would be needed to constrain the low-energy spectrum of the SNR. A hadronic scenario was also invoked for the SNR Monoceros Loop (Katagiri et al. 2016b). In this case, the brightest gamma-ray peak is spatially correlated with the Rosette Nebula, a young stellar cluster and MC complex located at the edge of the southern shell of the SNR which has a role similar to W3 for the HB 3/W3 complex. The interaction between the SNR and the MC provides the target to naturally produce gamma-rays via proton–proton interaction and it is not a surprise that we confirm a spectral break at low energy for the Monoceros SNR

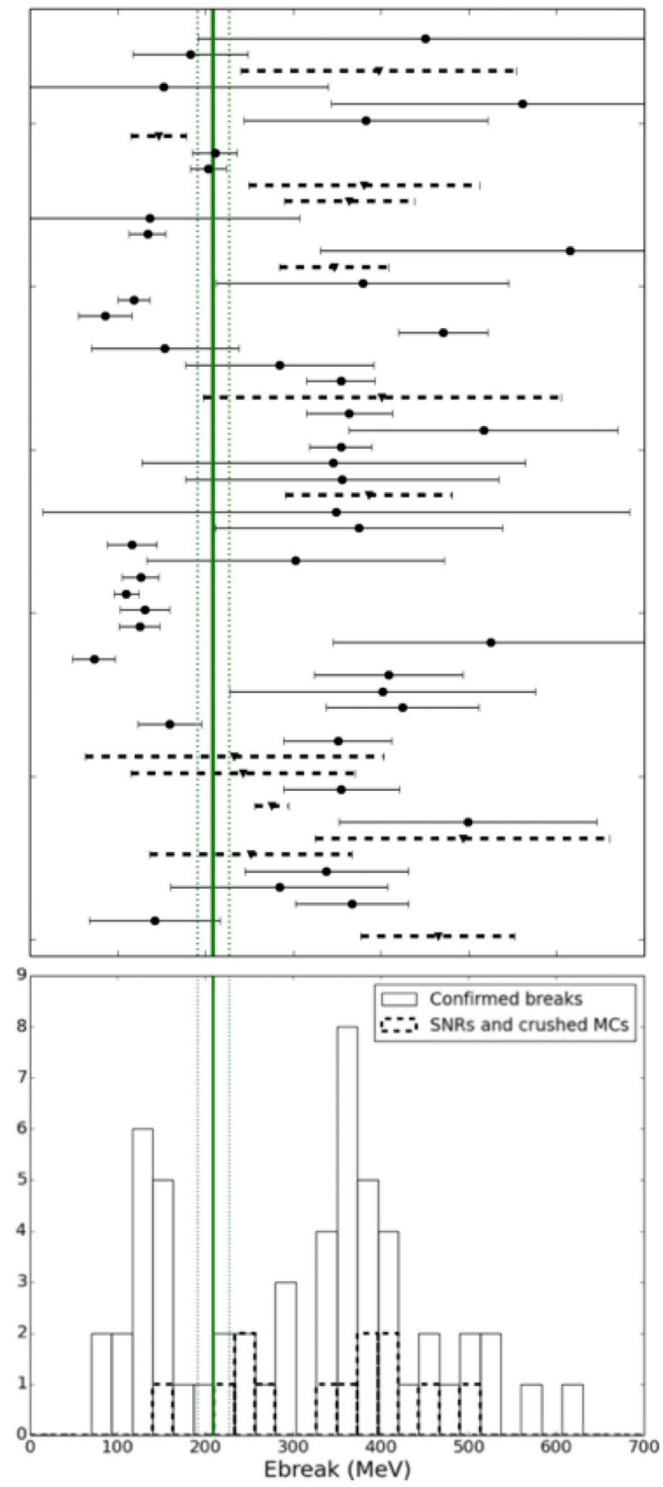


**Figure 7.** Break energy for the 56 sources confirmed by our studies of systematics (black line) and for the identified SNRs and/or crushed MCs (dotted line, see Section 4.2). The green line indicates the value of the break energy obtained using simulations based on the *naima* package for a proton injection index of 2.0 and the two green dotted–dashed lines indicate the $1\sigma$ confidence interval derived (more details in Appendix A). (Top) Individual values; (Bottom) Corresponding histograms.

(4FGL J0639.4+0655e, see Figure 11, bottom left) and for the Rosette complex (4FGL J0634.2+0436e, see Figure 11, middle right). More recently, modeling of the nonthermal emission of the gamma Cygni SNR (Fraija & Araya 2016; Fleischhack 2019), associated with the source 4FGL J2021.0+4031e, also suggested that the gamma-ray emission (analyzed above 100 MeV) might be of hadronic nature with enhanced gigaelectronvolt emission spatially coincident with the teraelectronvolt source VER J2019+407. Here again, our low-energy analysis detects a low-energy break in the spectrum of this SNR (see Figure 17, bottom right) but it should be noted that the bright gamma-ray emission from the pulsar PSR J2021+4026, lying near the center of the remnant, is very difficult to disentangle from the signal of the SNR at these low energies, which could lead to some contamination in the SNR spectrum. A follow-up study in the off pulse of the pulsar would therefore be needed to confirm the results obtained with our pipeline. This applies not only to supernova remnants but also to all sources coincident with (or very close to) a bright gamma-ray pulsar. It is even more clear for 4FGL J1514.2-5909e associated with the pulsar wind nebula MSH 15-52 and coincident with the soft gamma-ray pulsar PSR B1509-58. The very high low-energy flux visible in Figure 13 (bottom right) is most likely to the associated pulsar PSR B1509-58, which is not included in the 4FGL Catalog and would be hard to disentangle from the PWNe at these energies.

### 4.3. Constraints on Other Identified Sources

As discussed in Section 4.2, gamma-ray observations are suggestive of hadron acceleration in a number of SNRs: the young SNRs Tycho and Cassiopeia A, and the middle-aged remnants with pion-decay signature cited above. However, definite proof of proton acceleration, especially at petaelectronvolt energies, is still missing and alternative Galactic sources of cosmic rays could play a significant role.

The shocks generated by the stellar winds of massive stars or star-forming regions are among these cosmic-ray accelerators. In this respect, the detection of gamma-rays of the Cygnus region by the LAT (Ackermann et al. 2011) opened new perspectives by revealing the presence of a cocoon of freshly accelerated cosmic rays over a scale of ∼50 pc. Our analysis revealed a spectral break for the SFR analyzed, 4FGL J2028.6+4110e (see Figure 18, top left), which is associated with the cocoon. A very hard index $\Gamma_1 = 1.00 \pm 0.02_{\rm stat} \pm 0.37_{\rm syst}$ is detected up to break energy at $383 \pm 13_{\rm stat} \pm 138_{\rm syst}$ MeV, followed by a spectral index $\Gamma_2 = 2.23 \pm 0.06_{\rm stat} \pm 0.24_{\rm syst}$, similar to those observed for the population of identified SNRs as can be seen in Figure 8. Complete modeling of the source at gamma-ray energies is beyond the scope of this paper but our results tend to favor the hadronic scenario, thus reinforcing the long-standing hypothesis that massive SFRs house particle accelerators.

Gamma-ray binaries, microquasars, and colliding wind binaries could also contribute to the sea of Galactic cosmic rays and at least contribute significantly to the population of sources with significant breaks as reported in Section 4.1. Spectral breaks have been detected for these three types of sources with 4FGL J0240.5+6113 associated with the high-mass gamma-ray binary (HMB) LS I+61 303 (Figure 10, top right), the HMB 4FGL J1018.9−5856 (Figure 12, bottom left), 4FGL J1045.1-5940 associated with the colliding wind binary $\eta$ Carinae (Figure 12, bottom right) and 4FGL J2032.6+4053 associated with the microquasar Cyg X-3 (Figure 18, top right). However, this last source presents the highest value of spectral index $\Gamma_1$ ($1.90 \pm 0.16_{\rm stat} \pm 0.07_{\rm syst}$) among the 56 candidates, which does not really look like the standard *pion bump*

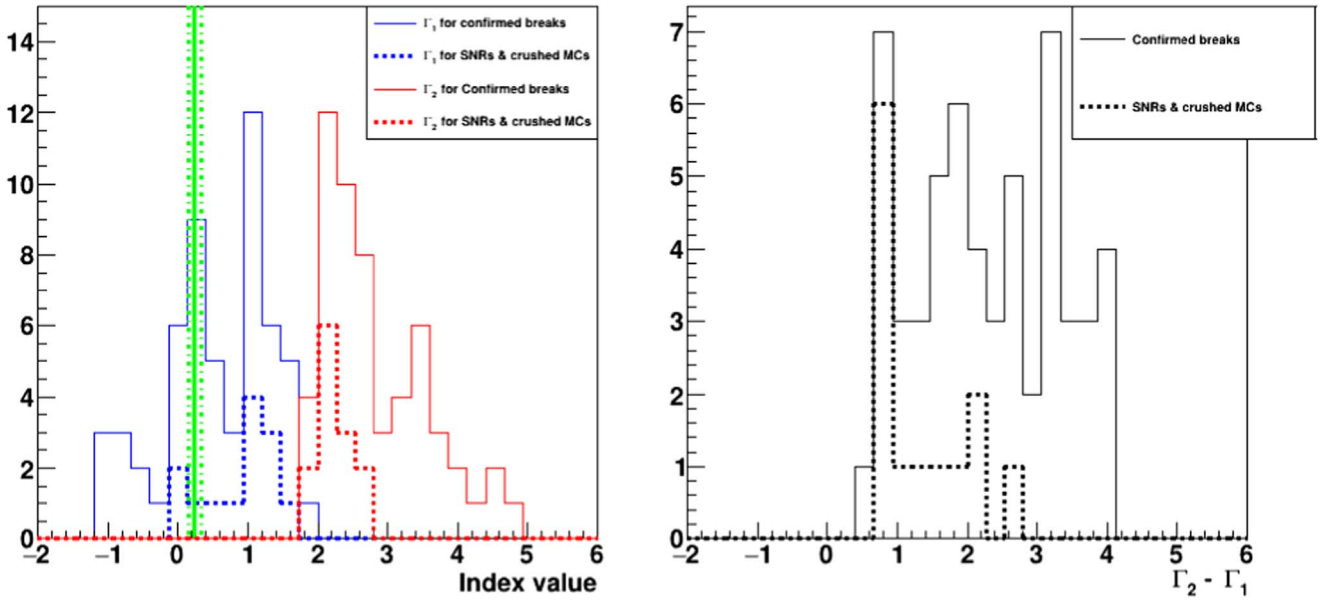


**Figure 8.** $\Gamma_1$ (blue line, left), $\Gamma_2$ (red line, left), and $\Gamma_2 - \Gamma_1$ (right) distributions for the 56 sources confirmed by our studies of systematics. In all cases, the dotted line corresponds to the same distribution presented with the solid line but restricted to SNRs (see Section 4.2). The green line indicates the value of $\Gamma_1$ obtained using simulations based on the *naima* package for a proton injection index of 2.0 and the two green dotted–dashed lines indicate the $1\sigma$ confidence interval derived (more details in Appendix A).

signature observed for interacting SNRs. Finally, the source 4FGL J1405.1-6119 was recently identified as a high-mass gamma-ray binary using Fermi-LAT observations (Corbet et al. 2019), and should therefore be added to the small set of gamma-ray binaries detected in our analysis. Since significant variability was detected by the LAT for these five gamma-ray sources, an individual analysis taking into account their orbital period would be needed to see if the spectral break detected is a signature of proton–proton acceleration.

### 4.4. Interesting New Cases: Potential Proton Accelerators?

Among the sources for which a significant spectral break is detected with our pipeline, several are classified as SPP, UNK, or even unassociated as can be seen in Table 5. Among these three source classes, SPP is the only one for which the fraction of sources with significant break is similar to the analyzed fraction (11.9% versus 10.7%), while UNK and UNIDs both show a clear decrease between the analyzed fraction and the confirmed one (see Figure 5). The SPP are sources of unknown nature but overlapping with known SNRs or PWNe and thus candidates to these classes, while UNK are sources associated with counterparts of unknown nature. Unassociated, SPP and UNK represent 29.7% of the 4FGL sources: revealing the mystery of the nature of these unidentified gamma-ray sources might shed new light on the problem of the origin of Galactic cosmic rays. In this respect, three sources detected by our pipeline are of special interest since they are coincident with SNRs and/or dense molecular clouds.

This is the case for 4FGL J1601.3-5224 (Figure 14, middle right) coincident with the SNR G329.7+00.4, which presents a diffuse shell at radio energies (Whiteoak & Green 1996) but is not detected at any other wavelength. Our analysis indicates a soft spectrum $\Gamma_2 = 3.78 \pm 0.32_{\rm stat} \pm 0.89_{\rm syst}$ with large systematics due to the diffuse background. The same systematics affect the value of the energy break showing that our results may suffer from contamination.

Similarly, the source 4FGL J1934.3+1859 (Figure 17, bottom left) is coincident with SNR G054.4-00.3 detected as a nearly circular shape and angular diameter of $\sim 40'$ at radio energies (Junkes et al. 1992) while Swift and Suzaku X-ray observations allowed for the detection of the X-ray counterpart (Karpova et al. 2017) of the gamma-ray pulsar PSR J1932+1916 (Pletsch et al. 2013) located near the edge of the SNR. Suzaku observations also revealed diffuse emission with an extent of about $5'$ whose spectral properties are compatible with those of PSR+PWN systems. Interestingly, large-scale CO structures across the SNR were observed, indicating the SNR interaction with the ambient molecular gas, which is an important ingredient to enhance the gamma-ray emission due to proton–proton interaction. Our analysis reveals a spectral index above the break energy $\Gamma_2 = 3.13 \pm 0.27_{\rm stat} \pm 0.12_{\rm syst}$, which may again indicate that the association with an SNR is spurious or that our low-energy analysis suffers from contamination from other neighboring sources in this crowded region.

Finally, the unidentified source 4FGL J1931.1+1656 (Figure 17, middle right) is coincident with the SNR candidate G52.37-0.70 detected in a recent THOR+VGPS analysis (Anderson et al. 2017). However, the spectral index of $\alpha = 0.3 \pm 0.3$ using Very Large Array observations (Driessen et al. 2018) seems to indicate that this candidate is unlikely to be an SNR. The gamma-ray spectrum derived by our analysis resembles that of other SNRs and is not affected by large systematics especially the break energy $203 \pm 8 \pm 19$ and the spectral index above the break $\Gamma_2 = 2.64 \pm 0.10 \pm 0.04$. It is the best candidate for proton acceleration among these three potential SNR associations.

These three regions are extremely complex and would deserve a dedicated analysis at higher energy with Fermi to constrain their location and their association with the corresponding SNR, as well as a spectral analysis over a larger energy interval to definitively constrain the type of radiating particles.

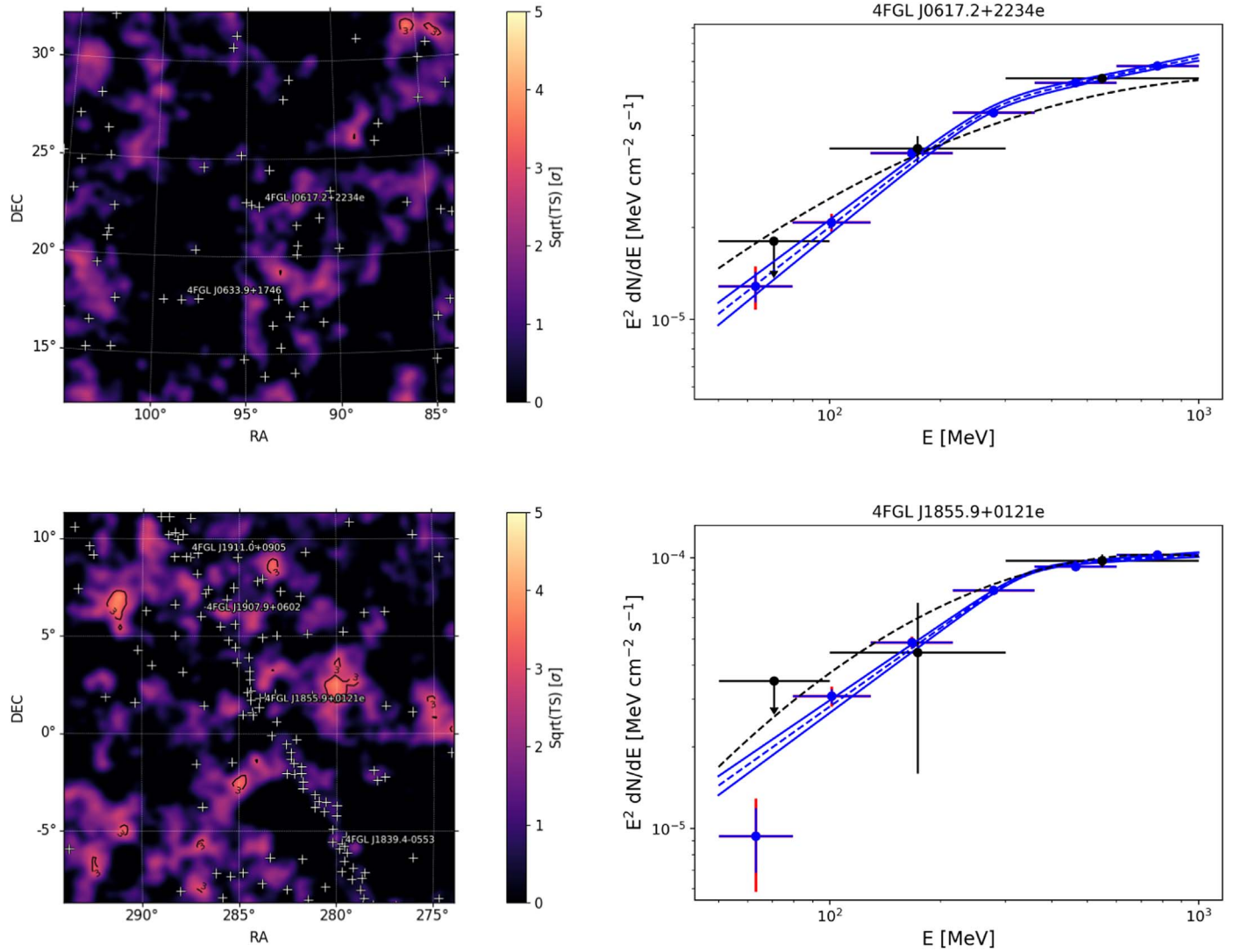


**Figure 9.** LAT residual TS maps in equatorial coordinates and significance units (left) and SEDs (right) of IC 443 (top) and W44 (bottom) between 50 MeV and 1 GeV. In the residual TS maps, all white crosses indicate the 4FGL sources included in the model of the region. For the SEDs, the blue points and butterflies are obtained in this analysis while the black points and dashed lines are from the 4FGL catalog. The red lines take into account both the statistical and systematic errors added in quadrature. A 95% C.L. upper limit is computed when the TS value is below 1.

Even more care should be taken for the extended sources 4FGL J1633.0-4746e (Figure 15, top left) and 4FGL J1813.1-1737e (Figure 15, bottom right) since their disk radii of 0.°61 and 0.°6, respectively, in confused Galactic plane regions adds to the complexity of such analysis at low energy. With its large extension, 4FGL J1633.0-4746e overlaps with both the teraelectronvolt PWN candidate HESS J1632-478 and the unidentified source HESS J1634-472, both detected at gigaelectronvolt energies but not included in our list of selected candidates due to their low significance at low energy. This implies that the region contains three sources: a point-like source coincident with HESS J1634-472, an extended source coincident with HESS J1632-478 but with an extension of 0.256° almost twice as large as the teraelectronvolt size, and the very extended source 4FGL J1633.0-4746e overlapping them detected above 10 GeV with a spectral index of $2.25 \pm 0.01_{\rm stat} \pm 0.10_{\rm syst}$ (Ackermann et al. 2017). Interestingly, our spectral analysis indicates a break at $517 \pm 18_{\rm stat} \pm 252_{\rm syst}$ MeV followed by an index of $\Gamma_2 = 2.11 \pm 0.15_{\rm stat} \pm 0.12_{\rm syst}$ in agreement with the index detected above 10 GeV (though with very large systematics on the break energy due to the diffuse background). The break detected at low energy by our analysis, the hard spectral index $\Gamma_2$ consistent with the one detected at higher energy (which seems to indicate a flat spectrum over a large energy range) and the presence of dense clumps in this region traced $NH_3(1,1)$ emission (de Wilt et al. 2017) make this source a very interesting proton accelerator. A dedicated analysis would therefore be very valuable in this case.

The disk radius of $0.60 \pm 0.06^{\circ}_{\rm stat}$ of the Fermi source 4FGL J1813.1-1737e, coincident with the compact teraelectronvolt PWN candidate HESS J1813-178 (Gaussian size of $0.049 \pm 0.04°$ in H.E.S.S. Collaboration et al. 2018b), was first detected by Araya (2018). The authors reported a hard index of $2.07 \pm 0.09_{\rm stat}$ above 500 MeV compatible with the teraelectronvolt index. This spectrum is compatible with the spectral index $\Gamma_2 = 2.17 \pm 0.03_{\rm stat} \pm 0.42_{\rm syst}$ derived in our analysis. With such a large extension in the Galactic plane, several sources could contribute to the gigaelectronvolt signal: the PWN powered by PSR J1813-1749 thought to emit at

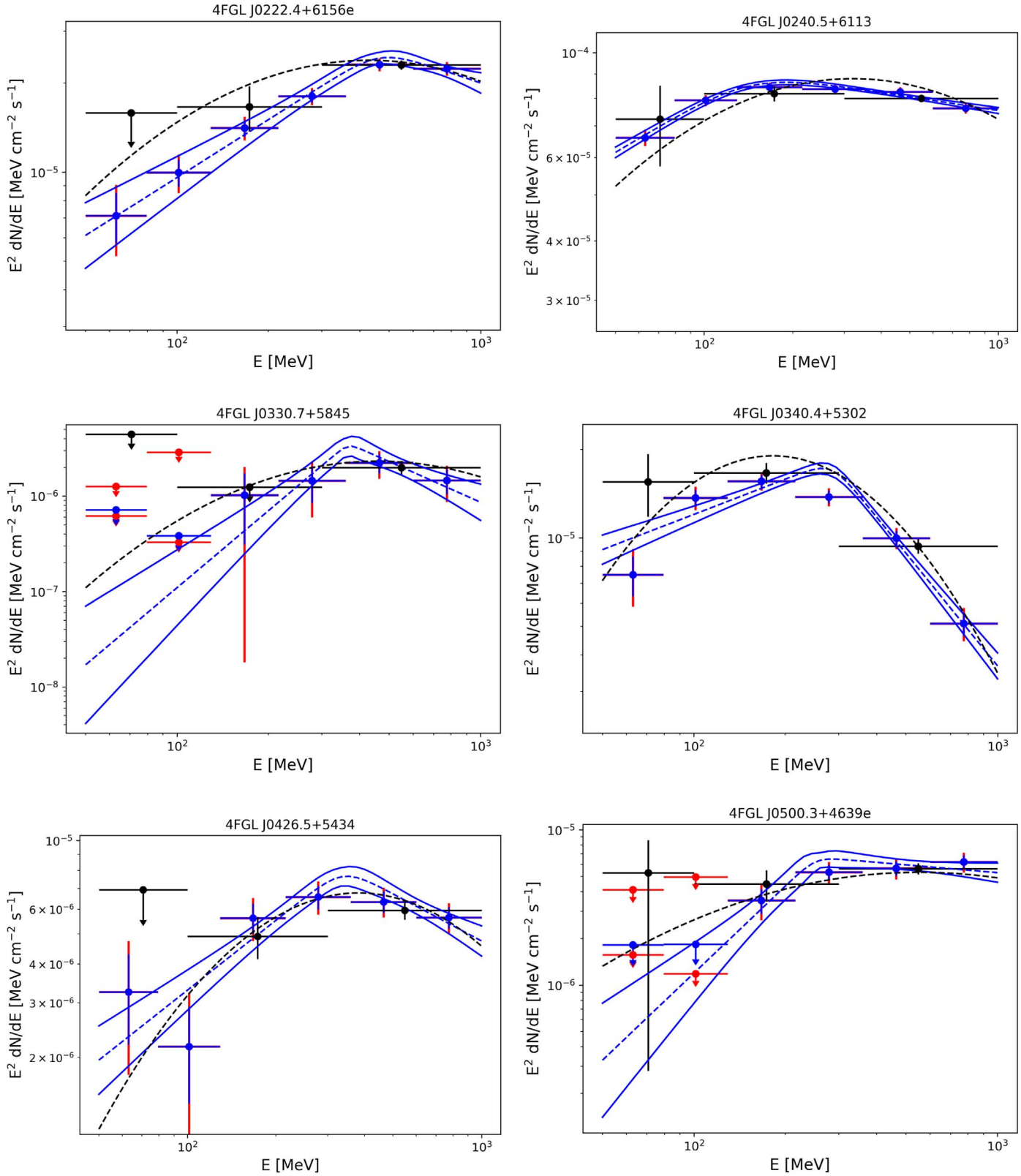


**Figure 10.** LAT SEDs of 4FGL J0222.4+6156e (top left), 4FGL J0240.5+6113 (top right), 4FGL J0330.7+5845 (middle left), 4FGL J0340.4+5302 (middle right), 4FGL J0426.5+5434 (bottom left), and 4FGL J0500.3+4639e (bottom right) with the same conventions used in Figure 9.

teraelectronvolt energies as seen by H.E.S.S. and HAWC (Abeysekara et al. 2017), the SNR G12.82-0.02 whose contribution to the teraelectronvolt signal was explored by Funk et al. (2007) and the giant SFR W33 that comprises a region of 15′ at a distance of 2.4 kpc (Immer et al. 2013). This last hypothesis was considered by Araya (2018), showing that the energetics, extended morphology, and spectrum of the gigaelectronvolt emission are similar to those of the other

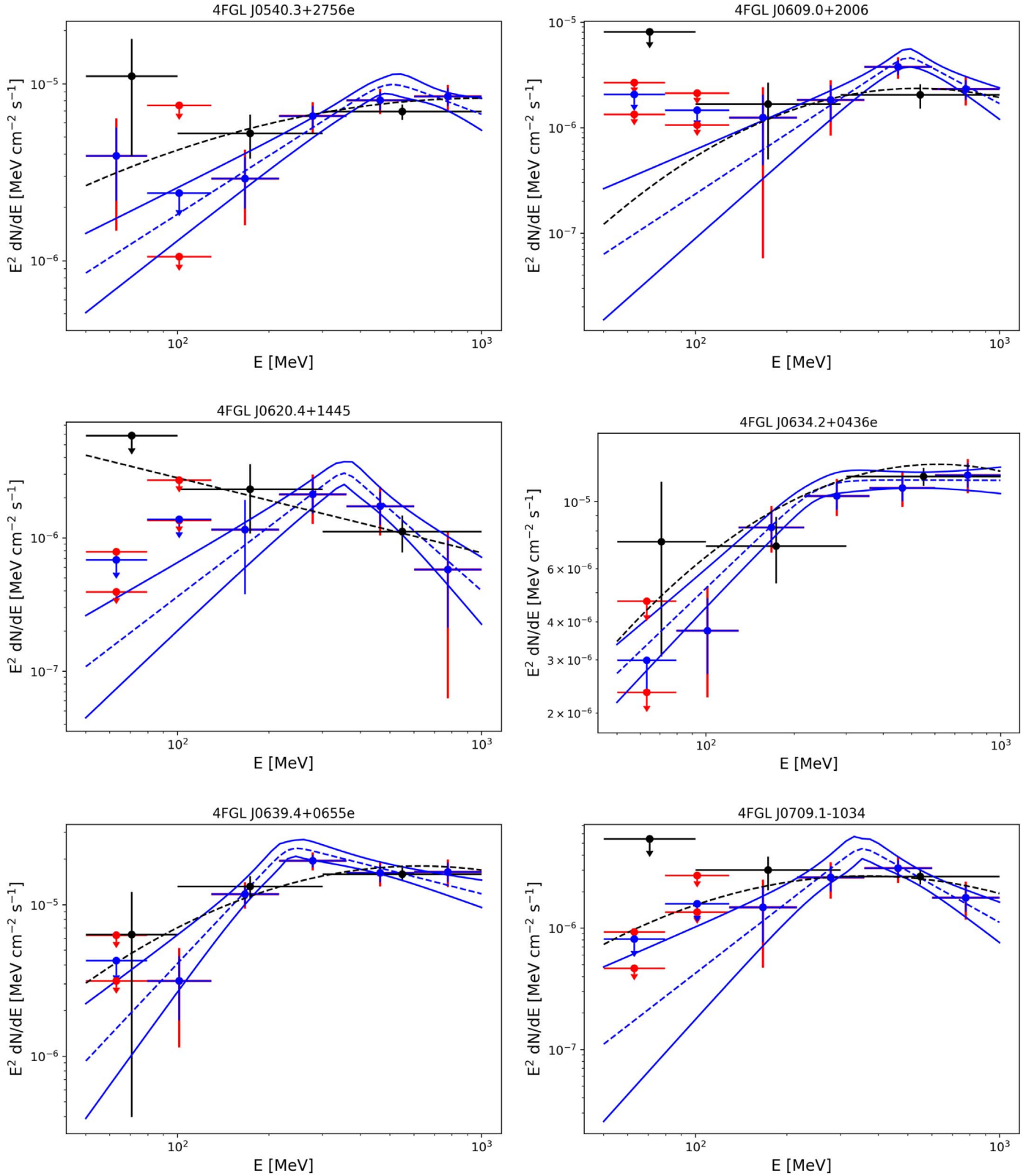


**Figure 11.** LAT SEDs of 4FGL J0540.3+2756e (top left), 4FGL J0609.0+2006 (top right), 4FGL J0620.4+1445 (middle left), 4FGL J0634.2+0436e (middle right), 4FGL J0639.4+0655e (bottom left), and 4FGL J0709.1−1034 (bottom right) with the same conventions used in Figure 9.

gamma-ray detected SFR, the Cygnus Cocoon. To firmly establish the presence of protons radiating at gamma-ray energies, such a complex region definitively is worth an individual analysis above 1 GeV to constrain the morphology and a spectral analysis over a larger energy range to model the broadband emission.

Finally, several sources detected by our analysis are completely unassociated and follow-up observations at

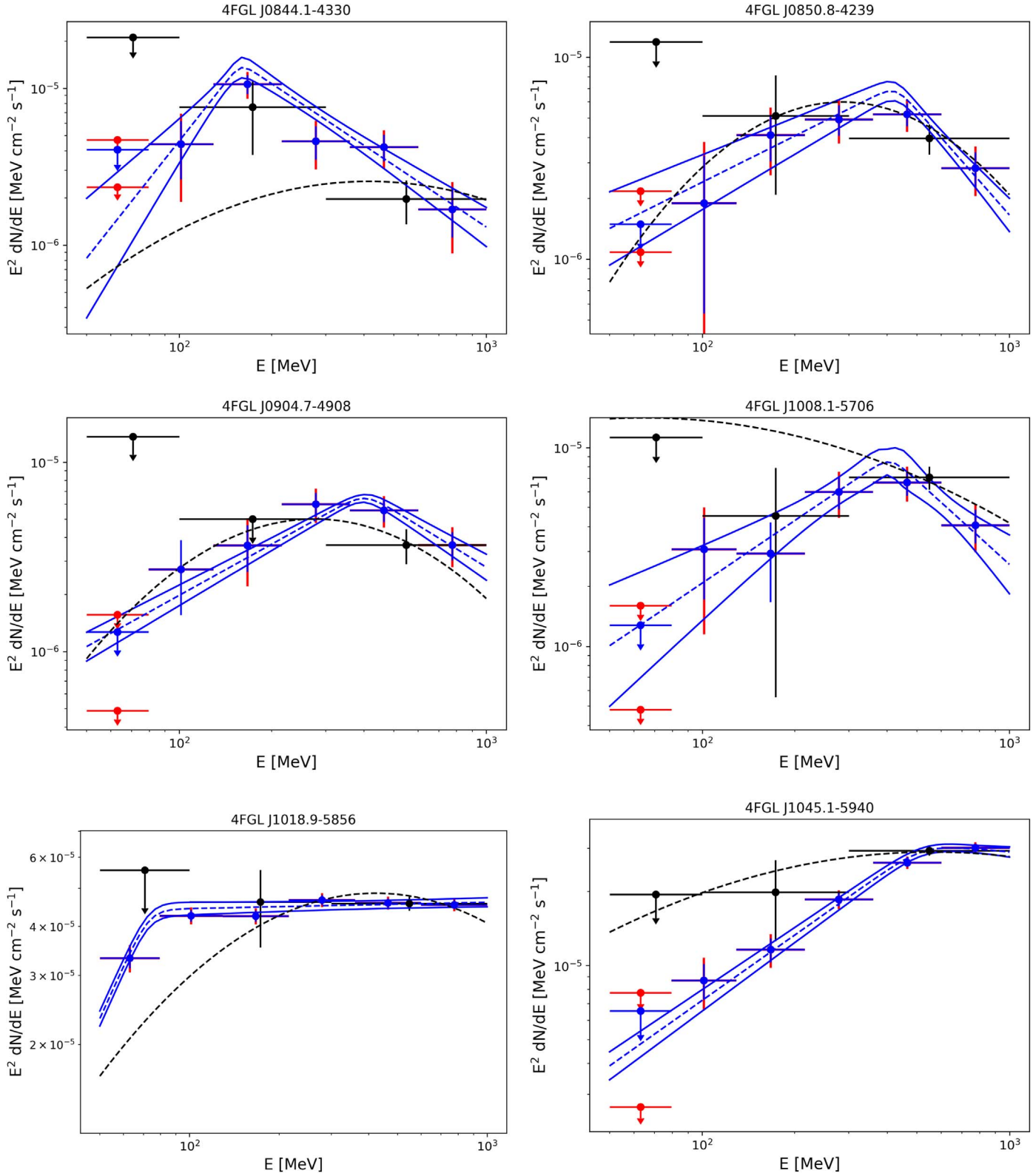


**Figure 12.** LAT SEDs of 4FGL J0844.1-4330 (top left), 4FGL J0850.8-4239 (top right), 4FGL J0904.7-4908 (middle left), 4FGL J1008.1-5706 (middle right), 4FGL J1018.9-5856 (bottom left), and 4FGL J1045.1-5940 (bottom right) with the same conventions used in Figure 9.

teraelectronvolt energies and X-rays would be needed to constrain their nature. They all present values of $\Gamma_2$ much softer than those of the identified SNRs discussed in Section 4.2. Similarly, the values of $\Gamma_2 - \Gamma_1$ obtained in our analysis are much larger ($\geqslant 2.96$) than those of the identified SNRs and dense MC regions. This tends to indicate that these sources are not associated with SNR shock acceleration.

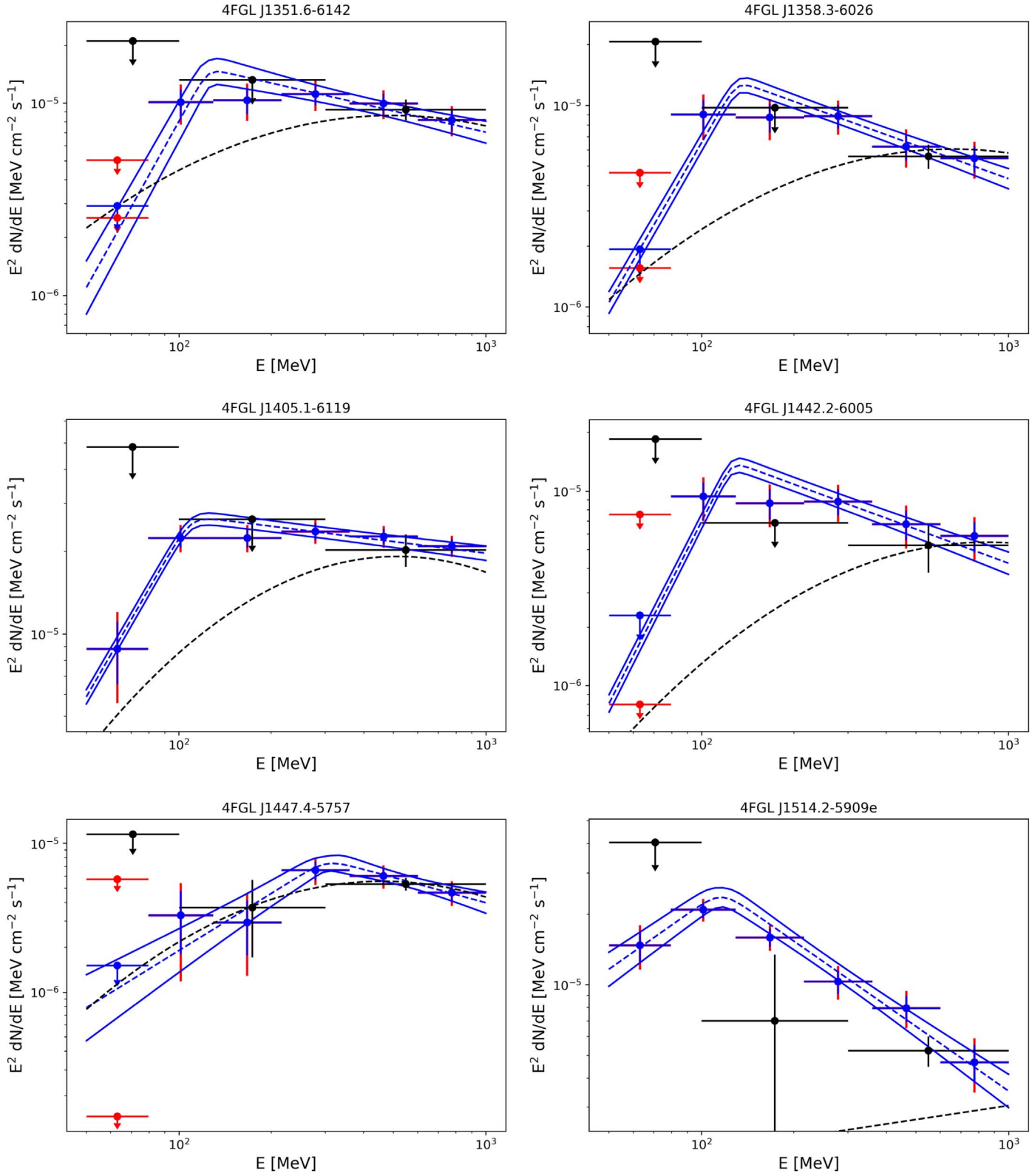


**Figure 13.** LAT SEDs of 4FGL J1351.6-6142 (top left), 4FGL J1358.3-6026 (top right), 4FGL J1405.1-6119 (middle left), 4FGL J1442.2-6005 (middle right), 4FGL J1447.4-5757 (bottom left), and 4FGL J1514.2-5909e (bottom right) with the same conventions used in Figure 9.

## 5. Summary

Using 8 yr of Pass 8 LAT data between 50 MeV and 1 GeV, we have analyzed 311 4FGL sources located within 5° from the Galactic plane and detected 77 sources with significant spectral breaks. We carried out a thorough study of the systematics associated with the diffuse Galactic background and with the effective area for each of them and we confirmed the spectral break for 56 of them. With 13 SNRs identified within this

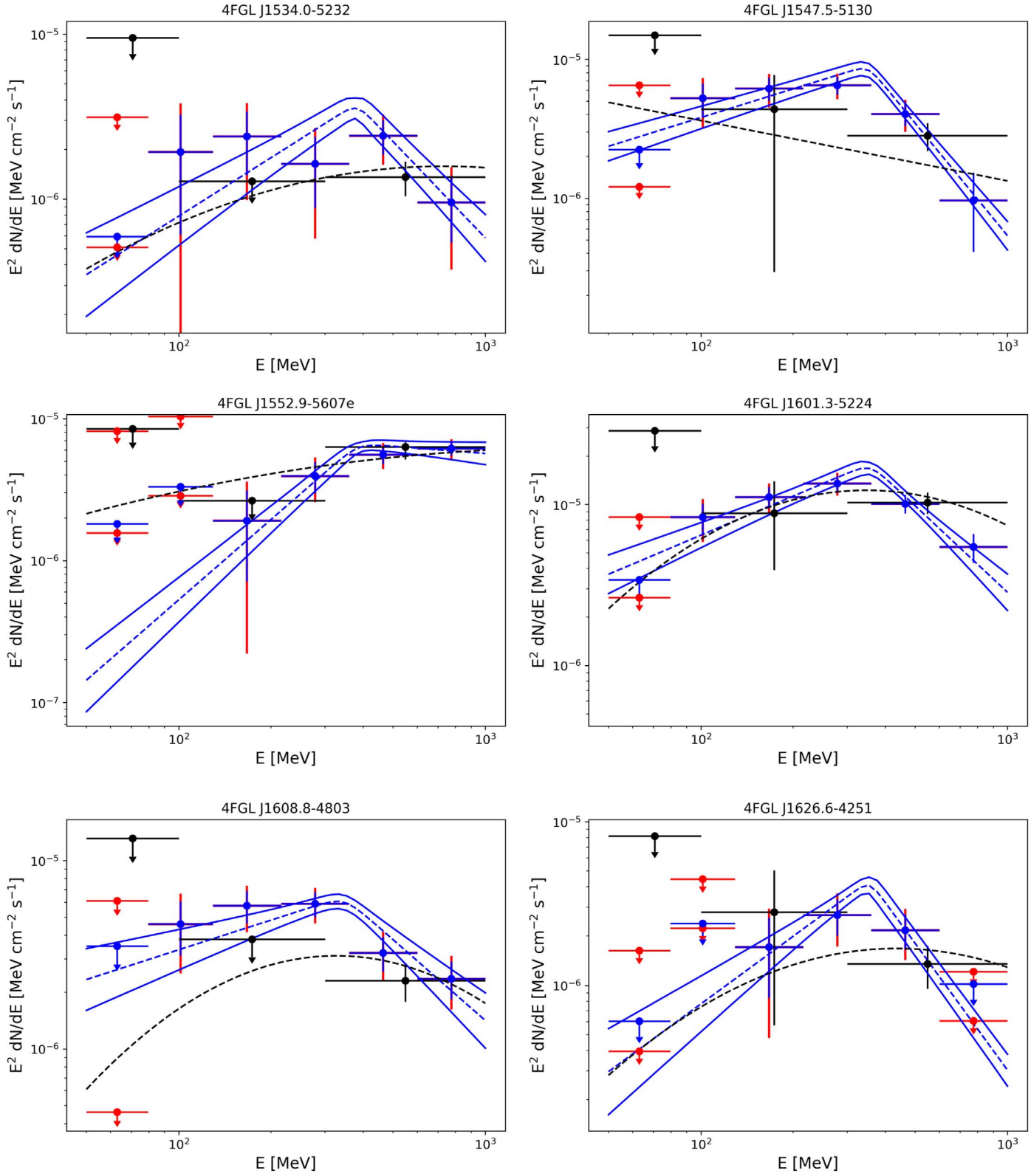


**Figure 14.** LAT SEDs of 4FGL J1534.0-5232 (top left), 4FGL J1547.5-5130 (top right), 4FGL J1552.9-5607e (middle left), 4FGL J1601.3-5224 (middle right), 4FGL J1608.8-4803 (bottom left), and 4FGL J1626.6-4251 (bottom right) with the same conventions used in Figure 9.

sample of 56 sources, SNRs are the dominant class of sources showing significant breaks at low energy. Only five binaries are included in the sample of 311 sources analyzed but four of them show a significant break at low energies. This seems to indicate that binaries could also have a significant contribution. The spectral characteristics were also evaluated for these 56 sources. The break energy of the sources ranges uniformly between 100 MeV and 550 MeV. However, a clear pattern is

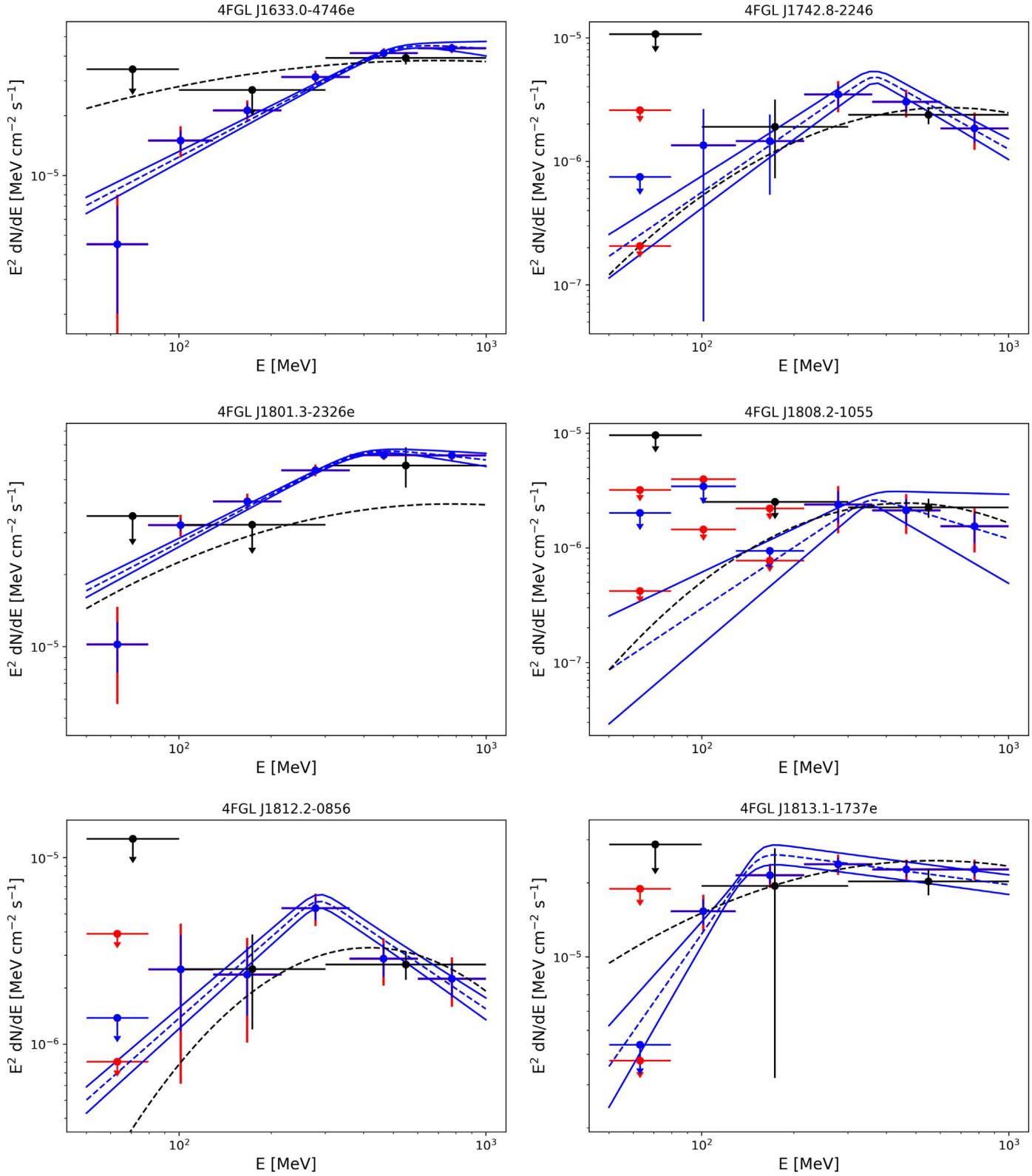


**Figure 15.** LAT SEDs of 4FGL J1633.0-4746 (top left), 4FGL J1742.8-2246 (top right), 4FGL J1801.3-2326e (middle left), 4FGL J1808.2-1055 (middle right), 4FGL J1812.2-0856 (bottom left), and 4FGL J1813.1-1737e (bottom right) with the same conventions used in Figure 9.

detected in the spectral index $\Gamma_2$ of the sources, which tends to center at 2.3 for the population of 13 identified SNRs. Similarly, the value of $\Gamma_2 - \Gamma_1$ tends to center at $\sim$1 for the same population of sources. This provides an interesting way to constrain the nature of the radiating particles. Our analysis also provides three interesting new proton accelerator candidates: 4FGL J1931.1+1656 is coincident with the SNR candidate G52.37-0.70 detected in a recent THOR+VGPS analysis, the extended source 4FGL J1633.0-4746e overlapping the terae-lectronvolt PWN candidate HESS J1632-478 and the

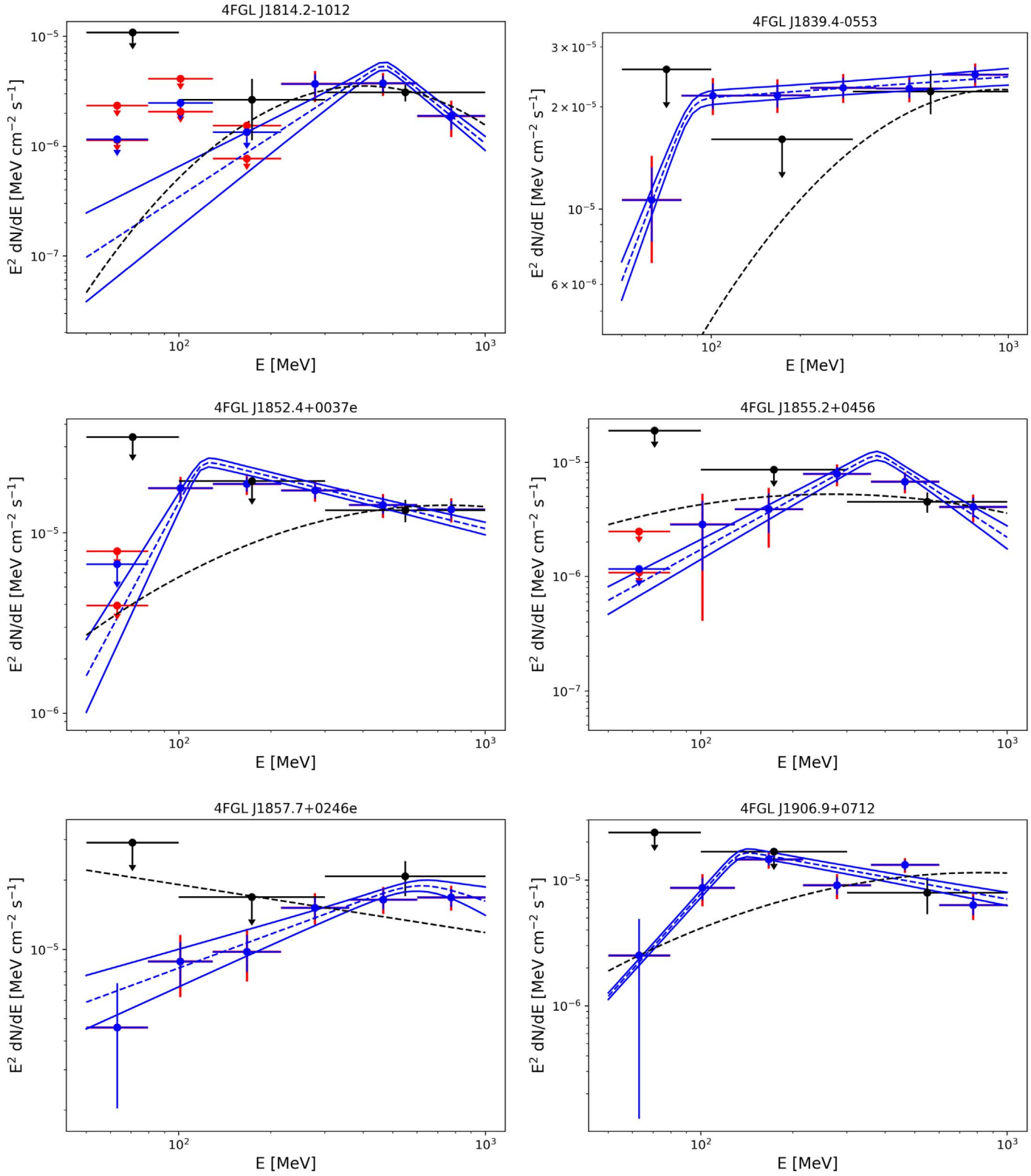


**Figure 16.** LAT SEDs of 4FGL J1814.2-1012 (top left), 4FGL J1839.4-0553 (top right), 4FGL J1852.4+0037e (middle left), 4FGL J1855.2+0456 (middle right), 4FGL J1857.7+0246e (bottom left), and 4FGL J1906.9+0712 (bottom right) with the same conventions used in Figure 9.

unidentified source HESS J1634-472, and the extended source 4FGL J1813.1-1737e coincident with the compact teraelectron-volt PWN candidate HESS J1813-178 and the SFR W33. The current and future observations of the LAT are thus crucial to probe the spectral characteristics of a source at low energy, providing excellent targets of proton acceleration for current and future Cherenkov telescopes such as CTA.

The Fermi-LAT Collaboration acknowledges generous ongoing support from a number of agencies and institutes that

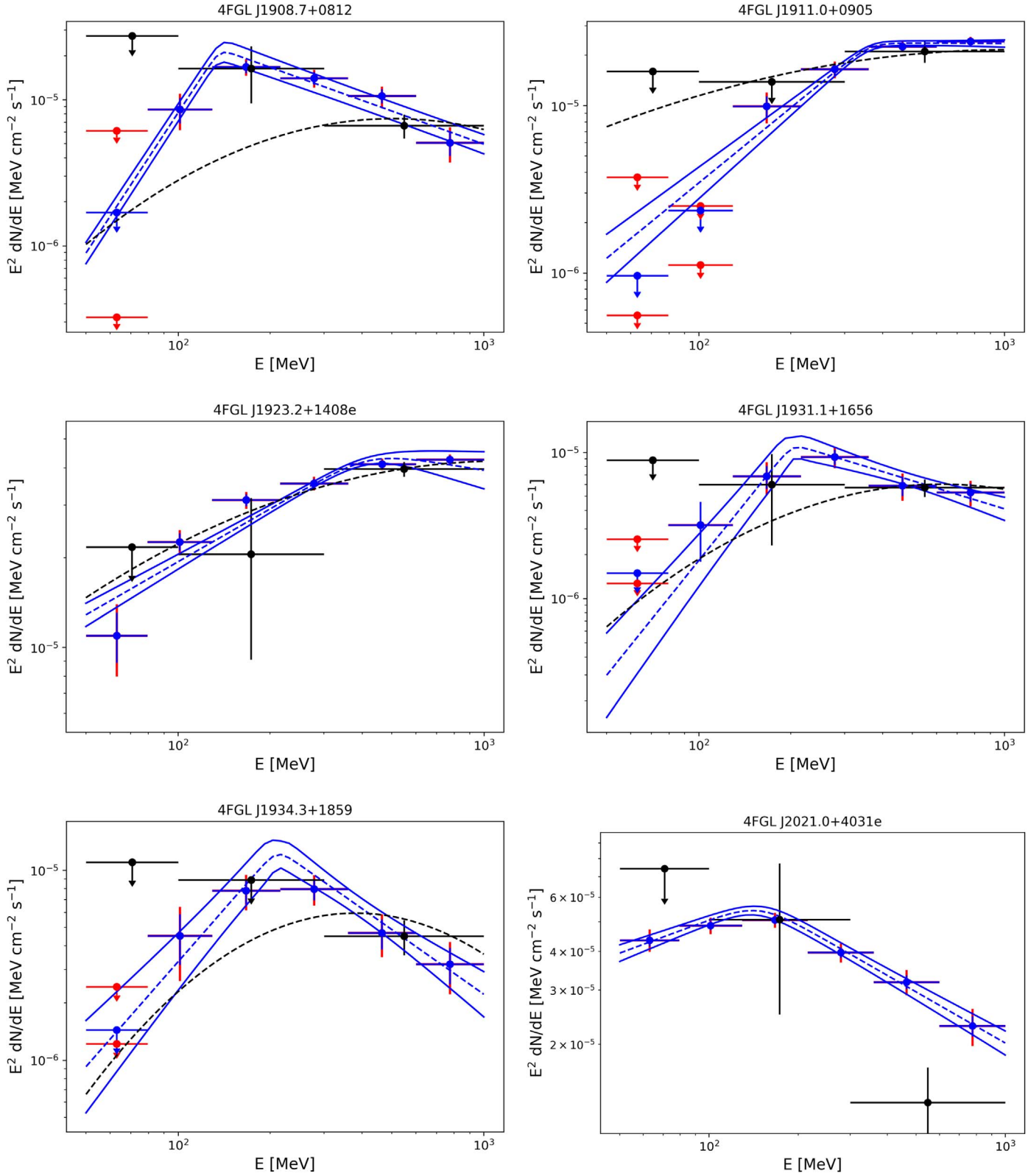


**Figure 17.** LAT SEDs of 4FGL J1908.7+0812 (top left), 4FGL J1911.0+0905 (top right), 4FGL J1923.2+1408e (middle left), 4FGL J1931.1+1656 (middle right), 4FGL J1934.3+1859 (bottom left), and 4FGL J2021.0+4031e (bottom right) with the same conventions used in Figure 9.

have supported both the development and the operation of the LAT as well as scientific data analysis. These include the National Aeronautics and Space Administration and the Department of Energy in the United States, the Commissariat à l'Energie Atomique and the Centre National de la Recherche Scientifique/Institut National de Physique Nucléaire et de Physique des Particules in France, the Agenzia Spaziale Italiana and the Istituto Nazionale di Fisica Nucleare in Italy, the Ministry of Education, Culture, Sports, Science and Technology (MEXT), High Energy Accelerator Research

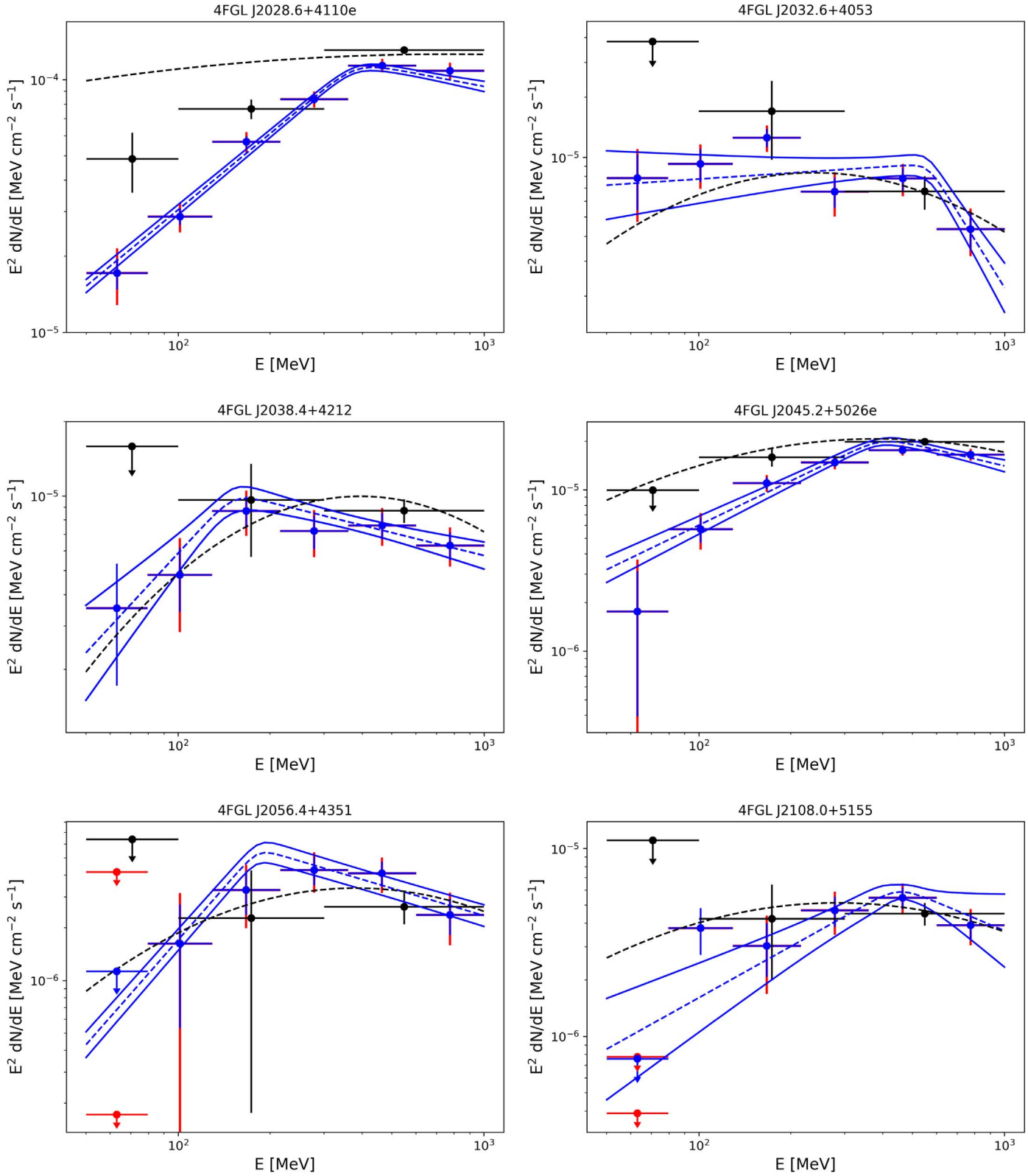


**Figure 18.** LAT SEDs of 4FGL J2028.6+4110e (top left), 4FGL J2032.6+4053 (top right), 4FGL J2038.4+4212 (middle left), 4FGL J2045.2+5026e (middle right), 4FGL J2056.4+4351 (bottom left), and 4FGL J2108.0+5155 (bottom right) with the same conventions used in Figure 9.

Organization (KEK) and Japan Aerospace Exploration Agency (JAXA) in Japan, and the K. A. Wallenberg Foundation, the Swedish Research Council and the Swedish National Space Board in Sweden. Additional support for science analysis during the operations phase is gratefully acknowledged from the Istituto Nazionale di Astrofisica in Italy and the Centre National d'Etudes Spatiales in France. Work at NRL is supported by NASA. M.L.G. acknowledges support from Agence Nationale de la Recherche (grant ANR- 17-CE31-0014).

## Appendix A
## The Pion-decay Bump Signature

As already discussed in the main text, when accelerated protons interact with the interstellar matter, they produce neutral pions which in turn decay into gamma-rays. This will create a characteristic signature at low energy in the gamma-ray spectrum called the pion-decay bump signature. To better understand how this signature is characterized in our energy interval of interest (50 MeV—1 GeV), we have used the python package *naima* (Zabalza 2015) to derive the gamma-ray emission produced by proton–proton interaction. To do so, *naima* uses an implementation of the analytical parameterizations of the energy spectra and production rates of gamma-rays from Kafexhiu et al. (2014), which is accurate within 20%. The inclusive $\pi^0$ production cross section is included as a combination of the experimental data cross sections at low energies, the Geant 4.10.0 cross section at intermediate energies and at higher energies the hadronic model Pythia 8.18 as the default. We applied *naima* to three different PL distributions of protons with spectral index $\Gamma_1$ varying between 1.5 and 2.5. The results presented in Figure A1 (left) are in perfect agreement with those published in Ackermann et al. (2013) and show that a very steep spectrum is expected below the break energy at ∼200 MeV. This figure also highlights that the pion-decay bump signature might be more difficult to detect for a hard proton distribution (red curve) than for steep injection spectra. This might in turn increase the systematic errors on the derived break energy. Finally, this figure demonstrates that the restricted energy interval of our analysis does not allow constraining the spectral index of the parent distribution since the gamma-ray spectra trace the energy distribution of parent protons at energies greater than 1 GeV. The upper bound of our energy interval was chosen since middle-aged SNRs commonly exhibit a high-energy spectral break at around 1–10 GeV (see the case of W28 with a break at 1 GeV reported by Abdo et al. 2010) and a simple broken PL model would not apply anymore above 1 GeV. To test for this effect, we applied *naima* to the same PL distributions of protons adding a break at 1 GeV in their distributions. We assumed that $\Gamma_2 = \Gamma_1 + 1$. Figure A1 (right) demonstrates that the break energy of the gamma-ray emission detected in our energy interval is not affected. However, this break significantly impacts the spectral index derived assuming a simple broken PL model. In a second step, we used the gamma-ray emission obtained with *naima* assuming a PL distribution of protons with $\Gamma_1 = 2.0$ and 2.5 to produce 200 Fermi simulated data files for each index over 8 yr using the *gtobssim* tool included in the LAT *fermitools*. We then analyzed these simulations using *fermitools* following the same procedure as

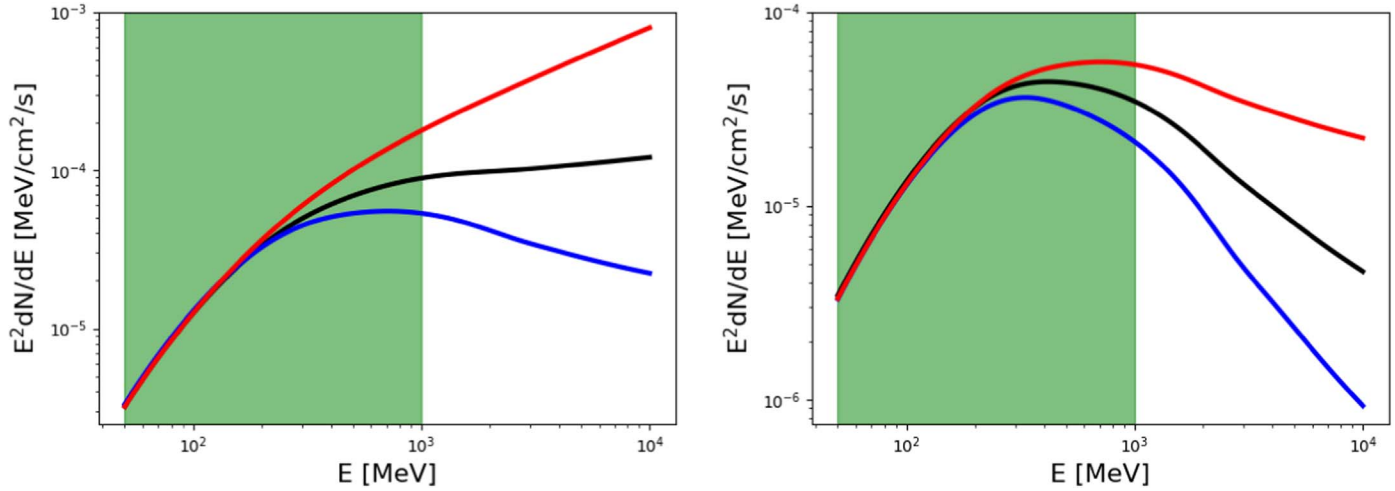


**Figure A1.** Left: gamma-ray spectra produced by a PL distribution of protons with spectral indices of 1.5 (red), 2.0 (black), and 2.5 (blue) as predicted by *naima* (Zabalza 2015). Right: same figure assuming that an energy break is present in the particle distribution at 1 GeV. The energy interval analyzed in this work is defined by the green area.

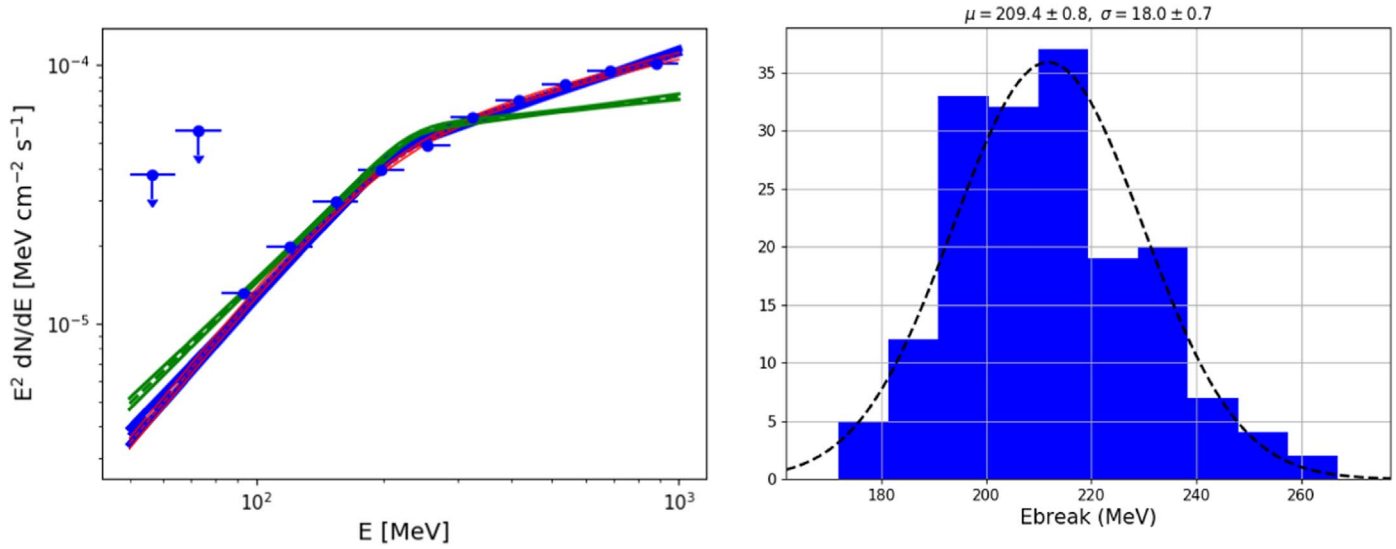


**Figure A2.** Left: gamma-ray spectrum derived using our analysis pipeline from one simulation of a PL distribution of protons with a spectral index of 2.0 predicted by *naima* (Zabalza 2015). The fit assuming a smooth broken PL model (see Equation (1)) with $\alpha = 0.1$ is represented by the blue curve. The fit assuming $\alpha = 0.5$ is represented by the red curve. The best fit of a similar simulation assuming a proton injection index of 2.5 is represented by the green line. Right: Distribution of the 200 values of energy break fitted for a proton injection spectral index of 2.0. The black line represents our best Gaussian fit.

**Table A1**
Results of The Gaussian Fits of the 200 *naima* Simulations Assuming Proton Injection Spectral Indices of 2.0 and 2.5

| | Proton Index = 2.0 | Proton Index = 2.5 |
|---|---|---|
| Energy break | 209/18 | 212/15 |
| $\Gamma_1$ | 0.24/0.09 | 0.29/0.09 |
| $\Gamma_2$ | 1.43/0.04 | 1.74/0.04 |

**Note.** The first column indicates the parameter fitted (energy break, $\Gamma_1$ and $\Gamma_2$), the second and third columns present the mean and sigma of the distribution obtained for a proton injection of 2.0 and 2.5, respectively.

with the real data, assuming a smooth broken PL spectral model with $\alpha = 0.1$ (see Equation (1)), except that the SED was produced for 12 energy bins instead of 6 to reflect the high statistics of our simulations (which mimics the flux of IC 443). We did not introduce any diffuse background in our simulations to clearly show how a proton spectrum will be reconstructed at low energies with the LAT in the absence of systematic errors. Figure A2 presents the gamma-ray spectrum derived for one of these simulations demonstrating that the spectral index derived above the break does not trace the parent proton distribution. The error bars are extremely small due to the high flux of the simulated source and the absence of diffuse background. This figure also shows that the smooth broken PL model used in our analysis with $\alpha = 0.1$ reproduces the gamma-ray spectrum well. A smoothness parameter $\alpha = 0.5$ was also tested but it does not significantly improve the likelihood of the fit. Finally, one can see that the injection spectral index does not seem to impact the break energy and the index $\Gamma_1$ of our smooth broken PL fit. The only parameter affected is the index $\Gamma_2$. To confirm this trend, we plotted the distributions of the 200 reconstructed values of the break energy, $\Gamma_1$ and $\Gamma_2$ for each injection spectral index, and fitted a Gaussian on each distribution as can be seen in Figure A2 (right) for the case of the break energy. The results are presented in Table A1 confirming that the only parameter affected by the different injection spectral indices is $\Gamma_2$. This study demonstrates that no steep spectrum is predicted for a standard injection spectral index. The only way to produce the steep spectra observed for some of the candidates detected in our analysis would be to include an energy break at (or below) 1 GeV in the injection proton spectrum as shown in Figure A1 (right).

## Appendix B
## List of the 311 Galactic Plane Sources Analyzed

Table B1 provides the list of all candidates analyzed. Columns 2 and 3 provide the Galactic longitude and latitude of the 311 candidates. Columns 4, 5, and 6 provide the curvature significance, the significance between 300 MeV and 1 GeV and the source class reported in the 4FGL catalog. Columns 7–10 provide the values obtained in our analysis concerning the TS of each source, the improvement of the log-normal representation with respect to the PL model $TS_{LP}$ as defined in Section 3.2, the improvement of the smooth broken PL representation with respect to the PL model $TS_{SBPL}$ and the improvement of the smooth broken PL representation when fixing $\Gamma_2 = 2$ called $TS_{SBPL2}$.

**Table B1**
List of Selected Galactic Plane Candidates

| 4FGL Name | GLON (°) | GLAT (°) | 4FGL SigCurv | 4FGL $\sqrt{TS}$ (0.3–1 GeV) | 4FGL Class | TS | $TS_{LP}$ | $TS_{SBPL}$ | $TS_{SBPL2}$ |
|---|---|---|---|---|---|---|---|---|---|
| 4FGL J0034.6+6438 | 121.13 | 1.83 | 2.6 | 3.9 | | 7.6 | | | |
| 4FGL J0039.1+6257 | 121.54 | 0.12 | 7.0 | 5.2 | | 43.8 | 7.0 | | |
| 4FGL J0129.0+6312 | 127.16 | 0.65 | 3.1 | 5.7 | spp | 55.9 | 5.1 | | |
| 4FGL J0142.5+6650 | 127.93 | 4.46 | 3.4 | 3.6 | | 6.4 | | | |
| 4FGL J0144.3+5959 | 129.51 | −2.20 | 0.6 | 3.4 | | 4.9 | | | |
| 4FGL J0211.5+6219 | 132.09 | 0.89 | 1.1 | 3.5 | | 0.3 | | | |
| 4FGL J0221.4+6241e | 133.05 | 1.60 | 5.7 | 8.8 | SNR | 75.9 | 0.5 | | |
| ⋆4FGL J0222.4+6156e | 133.42 | 0.94 | 14.3 | 30.7 | snr | 1307.1 | 27.2 | 34.8 | 32.4 |
| 4FGL J0235.3+5650 | 136.82 | −3.19 | 4.1 | 7.6 | | 77.1 | 3.7 | | |
| ⋆4FGL J0240.5+6113 | 135.68 | 1.09 | 28.2 | 107.3 | HMB | 39495.7 | 127.8 | 127.3 | 100.9 |

**Note.** Table B1 is published in its entirety in the machine-readable format. A portion is shown here for guidance regarding its form and content.
(This table is available in its entirety in machine-readable form.)

## ORCID iDs

F. Acero https://orcid.org/0000-0002-6606-2816
L. Baldini https://orcid.org/0000-0002-9785-7726
J. Ballet https://orcid.org/0000-0002-8784-2977
D. Bastieri https://orcid.org/0000-0002-6954-8862
R. Bellazzini https://orcid.org/0000-0002-2469-7063
E. Bissaldi https://orcid.org/0000-0001-9935-8106
R. D. Blandford https://orcid.org/0000-0002-1854-5506
R. Bonino https://orcid.org/0000-0002-4264-1215
R. A. Cameron https://orcid.org/0000-0003-0942-2747
P. A. Caraveo https://orcid.org/0000-0003-2478-8018
S. Ciprini https://orcid.org/0000-0002-0712-2479
F. D'Ammando https://orcid.org/0000-0001-7618-7527
N. Di Lalla https://orcid.org/0000-0002-7574-1298
L. Di Venere https://orcid.org/0000-0003-0703-824X
A. Fiori https://orcid.org/0000-0003-3174-0688
Y. Fukazawa https://orcid.org/0000-0002-0921-8837
P. Fusco https://orcid.org/0000-0002-9383-2425
F. Gargano https://orcid.org/0000-0002-5055-6395
D. Gasparrini https://orcid.org/0000-0002-5064-9495
M. Giroletti https://orcid.org/0000-0002-8657-8852
T. Glanzman https://orcid.org/0000-0001-9649-3871
S. Guiriec https://orcid.org/0000-0001-5780-8770
A. K. Harding https://orcid.org/0000-0001-6119-859X
E. Hays https://orcid.org/0000-0002-8172-593X
J. W. Hewitt https://orcid.org/0000-0001-5254-2248
G. Jóhannesson https://orcid.org/0000-0003-1458-7036
M. Kerr https://orcid.org/0000-0002-0893-4073
M. Kuss https://orcid.org/0000-0003-1212-9998
S. Larsson https://orcid.org/0000-0003-0716-107X
L. Latronico https://orcid.org/0000-0002-0984-1856
M. Lemoine-Goumard https://orcid.org/0000-0002-4462-3686
F. Longo https://orcid.org/0000-0003-2501-2270
F. Loparco https://orcid.org/0000-0002-1173-5673
P. Lubrano https://orcid.org/0000-0003-0221-4806
S. Maldera https://orcid.org/0000-0002-0698-4421
A. Manfreda https://orcid.org/0000-0002-0998-4953
M. N. Mazziotta https://orcid.org/0000-0001-9325-4672
N. Mirabal https://orcid.org/0000-0002-7021-5838
W. Mitthumsiri https://orcid.org/0000-0002-3776-072X
T. Mizuno https://orcid.org/0000-0001-7263-0296
M. E. Monzani https://orcid.org/0000-0002-8254-5308
A. Morselli https://orcid.org/0000-0002-7704-9553
I. V. Moskalenko https://orcid.org/0000-0001-6141-458X
E. Nuss https://orcid.org/0000-0002-3528-5777
N. Omodei https://orcid.org/0000-0002-5448-7577
M. Persic https://orcid.org/0000-0003-1853-4900
M. Pesce-Rollins https://orcid.org/0000-0003-1790-8018
H. Poon https://orcid.org/0000-0002-6004-4270
G. Principe https://orcid.org/0000-0003-0406-7387
S. Rainò https://orcid.org/0000-0002-9181-0345
R. Rando https://orcid.org/0000-0001-6992-818X
B. Rani https://orcid.org/0000-0001-5711-084X
M. Razzano https://orcid.org/0000-0003-4825-1629
S. Razzaque https://orcid.org/0000-0002-0130-2460
A. Reimer https://orcid.org/0000-0001-8604-7077
O. Reimer https://orcid.org/0000-0001-6953-1385
M. Sánchez-Conde https://orcid.org/0000-0002-4462-3686
P. M. Saz Parkinson https://orcid.org/0000-0001-6566-1246
D. Serini https://orcid.org/0000-0002-9754-6530
C. Sgrò https://orcid.org/0000-0001-5676-6214
D. Tak https://orcid.org/0000-0002-9852-2469
D. F. Torres https://orcid.org/0000-0002-1522-9065
E. Troja https://orcid.org/0000-0002-1869-7817
J. Valverde https://orcid.org/0000-0002-8090-6528
Z. Wadiasingh https://orcid.org/0000-0002-9249-0515

## References

Abdo, A. A., Ackermann, M., Ajello, M., et al. 2010, ApJ, 718, 348
Abdollahi, S., Acero, F., Ackermann, M., et al. 2020, ApJS, 247, 33
Abeysekara, A. U., Albert, A., Alfaro, R., et al. 2017, ApJ, 843, 40
Acero, F., Ackermann, M., Ajello, M., et al. 2016, ApJS, 224, 8
Ackermann, M., Ajello, M., Allafort, A., et al. 2011, Sci, 334, 1103
Ackermann, M., Ajello, M., Allafort, A., et al. 2013, Sci, 339, 807
Ackermann, M., Ajello, M., Baldini, L., et al. 2017, ApJ, 843, 139
Ackermann, M., Ajello, M., Baldini, L., et al. 2018, ApJS, 237, 32
Ackermann, M., Ajello, M., Albert, A., et al. 2012, ApJS, 203, 70
Ambrogi, L., Zanin, R., Casanova, S., et al. 2019, A&A, 623, A86
Anderson, L. D., Wang, Y., Bihr, S., et al. 2017, A&A, 605, A58
Araya, M. 2014, MNRAS, 444, 860
Araya, M. 2018, ApJ, 859, 69
Atwood, W., Albert, A., Baldini, L., et al. 2013, arXiv:1303.3514
Atwood, W. B., Abdo, A. A., Ackermann, M., et al. 2009, ApJ, 697, 1071
Bregeon, J., Charles, E., & Wood, M. 2013, arXiv:1304.5456
Bruel, P., Burnett, T. H., Digel, S. W., et al. 2018, arXiv:1810.11394
Corbet, R. H. D., Chomiuk, L., Coe, M. J., et al. 2019, ApJ, 884, 93
de Wilt, P., Rowell, G., Walsh, A. J., et al. 2017, MNRAS, 468, 2093
Devin, J., Acero, F., Ballet, J., & Schmid, J. 2018, A&A, 617, A5
Driessen, L. N., Domček, V., Vink, J., et al. 2018, ApJ, 860, 133

Drury, L. O. 1983, RPPh, 46, 973
Esposito, J. A., Hunter, S. D., Kanbach, G., & Sreekumar, P. 1996, ApJ, 461, 820
Fleischhack, H. 2019, ICRC (Madison, WI), 36, 675, arXiv:1907.08572
Fraija, N., & Araya, M. 2016, ApJ, 826, 31
Funk, S., Hinton, J. A., Moriguchi, Y., et al. 2007, A&A, 470, 249
Giuliani, A., Cardillo, M., Tavani, M., et al. 2011, ApJL, 742, L30
H. E. S. S. Collaboration, Abdalla, H., Abramowski, A., et al. 2018a, A&A, 612, A5
H. E. S. S. Collaboration, Abdalla, H., Abramowski, A., et al. 2018b, A&A, 612, A1
Hanabata, Y., Katagiri, H., Hewitt, J. W., et al. 2014, ApJ, 786, 145
Helene, O. 1983, NIMPR, 212, 319
Immer, K., Reid, M. J., Menten, K. M., Brunthaler, A., & Dame, T. M. 2013, A&A, 553, A117
Jogler, T., & Funk, S. 2016, ApJ, 816, 100
Junkes, N., Fuerst, E., & Reich, W. 1992, A&A, 261, 289
Kafexhiu, E., Aharonian, F., Taylor, A. M., & Vila, G. S. 2014, PhRvD, 90, 123014
Karpova, A., Shternin, P., Zyuzin, D., Danilenko, A., & Shibanov, Y. 2017, MNRAS, 466, 1757
Katagiri, H., Yoshida, K., Ballet, J., et al. 2016a, ApJ, 818, 114
Katagiri, H., Sugiyama, S., Ackermann, M., et al. 2016b, ApJ, 831, 106
Katsuta, J., Uchiyama, Y., Tanaka, T., et al. 2012, ApJ, 752, 135
Pletsch, H. J., Guillemot, L., Allen, B., et al. 2013, ApJL, 779, L11
Stecker, F. W. 1971, Cosmic Gamma Rays, Vol. 249 (Baltimore, MD: Mono Book Corp.)
Uchiyama, Y., Blandford, R. D., Funk, S., Tajima, H., & Tanaka, T. 2010, ApJL, 723, L122
Whiteoak, J. B. Z., & Green, A. J. 1996, A&AS, 118, 329
Wood, M., Caputo, R., Charles, E., et al. 2017, ICRC (Bexco, Busan, Korea), 35, 824
Yuan, Y., Funk, S., Jóhannesson, G., et al. 2013, ApJ, 779, 117
Zabalza, V. 2015, ICRC (The Hague), 34, 922